Journal of Materials Research and Technology 41 (2026) 593–608

Contents lists available at ScienceDirect

Journal of Materials Research and Technology

journal homepage: www.elsevier.com/locate/jmrt

The impact of scanning strategy on cell structures in PBF-LB/M/IN718: an *in situ* synchrotron x-ray diffraction study

B. Ferrari [a,*], A. Fantin [a], D. Said [b], A.N. Fitch [c], P. Suárez Ocano [a], T. Mishurova [a], I. Roveda [a], A. Kromm [a], R. Darvishi Kamachali [a,d], G. Bruno [a,e], A. Evans [a], G. Requena [f,g], L. Agudo Jácome [a], I. Serrano-Munoz [a,**]

[a] Bundesanstalt für Materialforschung und -prüfung (BAM), Berlin, Germany
[b] Materialise GmbH, Bremen, Germany
[c] European Synchrotron Radiation Facility (ESRF), Grenoble, France
[d] Institute of Materials Physics, University of Münster, Münster, Germany
[e] Institute of Physics and Astronomy, University of Potsdam, Potsdam, Germany
[f] Institute for Frontier Materials on Earth and Space, German Aerospace Center (DLR), Cologne, Germany
[g] Metallic Structures and Materials Systems for Aerospace, RWTH Aachen University, Aachen, Germany

ARTICLE INFO

Keywords:
Additive manufacturing
Inconel 718
Synchrotron x-ray diffraction
Heat treatment
Laser powder bed fusion
Cellular microstructure

ABSTRACT

In additive manufacturing, any change of the process parameters, such as scanning strategy, directly affects the cooling rates, heat accumulation, and overall thermal history of the build. Consequently, parts built with different process parameters tend to have different levels of crystallographic texture, residual stress, and dislocation density. These features can influence the properties of the material and their development during post-processing operations. In this study, IN718 prisms were built by laser powder bed fusion (PBF-LB/M) using two different scanning strategies (continuous 67° rotations around the build direction, *ROT*, and alternating 0°/67° scans, *ALT*) to provide two different as-built conditions. *In situ* time-resolved synchrotron diffraction was performed during a solution heat treatment at 1027 °C for 1 h. *Ex situ* scanning electron microscopy was used to support and complement the *in situ* observations. An approach to quantify the effect of elemental microsegregation at the cell walls is developed based on the deconvolution of asymmetric γ-nickel matrix peaks. Following this approach, the scanning strategies are shown to affect the as-built fraction of cell walls in the material, resulting in a difference of approximately 5 %, in weight fraction, between ROT and ALT (19 % vs. 24 %, respectively). This microsegregation was observed to be rapidly homogenized during the heating ramp, and no significant changes to the peak shape in the γ peaks occurred during the isothermal part of the heat treatment, regardless of the scanning strategy.

1. Introduction

In recent years, additive manufacturing (AM) has been increasingly used for the production of IN718 parts both for research and industrial purposes [1,2]. AM allows the fabrication of near-net shape geometrically complex parts, which enhances freedom of design, *e.g.*, by enabling lighter lattice or hollow structures, while minimizing the need for machining [3]. In AM, the part is built based on a computer-aided design (CAD) 3D model by adding material – layer upon layer – until the desired component is obtained [4]. Within the metal AM umbrella, powder bed fusion by laser beam (PBF-LB/M) is the most widespread technique, as it allows greater spatial accuracy than other techniques, such as directed energy deposition or electron beam-based methods [4].

Inconel 718 (IN718) is particularly suitable for PBF-LB (and AM in general) because of its good weldability and wide use in the aerospace industry, where part weight and performance are critical factors [5]. However, the alloy processed by AM differs significantly from well-established cast or wrought IN718 in terms of microstructure and properties [6,7]. The high cooling rates that are characteristic of AM (of the order of 10^6 K/s in the case of PBF-LB, versus 10^3 K/s for casting [4])

* Corresponding author.
** Corresponding author.
E-mail addresses: bruno.ferrari@bam.de (B. Ferrari), itziar.serrano-munoz@bam.de (I. Serrano-Munoz).

https://doi.org/10.1016/j.jmrt.2025.11.214
Received 17 July 2025; Received in revised form 11 November 2025; Accepted 25 November 2025
Available online 27 November 2025

lead to a cellular solidification mode [8].

The cellular structure is widely reported in PBF-LB/M for various alloys and consists of generally columnar or otherwise elongated cellular substructures within the grains [4,9,10], where elemental microsegregation, primary phases, and dislocations are preferentially concentrated at the space between neighboring cells (i.e., the cell walls) [11,12]. Within each grain, the cells grow following the heat flow and the crystallographic directions of easiest growth – in the case of IN718, <100> [1,13]. In the as-built state, the primary phases found at the cell walls – as well as at low (L) and high (H) angle grain boundaries (AGBs) – are mainly the MC-type cubic (B1, Fm $\overline{3}$ m) carbides (M: Nb, Ti and Ta) and so-called "topologically close-packed" (TCP) $(Ni,Cr,Fe)_2(Nb,Mo,Ti)$ Laves (*Strukturbericht* designation: C14, space group: $P6_3/mmc$) [14–16]. Correspondingly, the microsegregated elements are primarily Nb and Mo; i.e. large and heavy atoms with low diffusivity [17–20].

Besides the distinct cellular structures and microsegregation, PBF-LB/M/IN718 is typically accompanied by high levels of residual stress (RS), which must be controlled via process parameter adjustment and/or post-processing [21–24]. The scanning strategy has been reported to impact the RS state, the cell wall interspacing, chemical heterogeneity, and precipitates in the as-built condition [20,25]. Generally, the two most widely used scanning strategies consist of parallel scans on each layer with: 1) a 67° rotation between consecutive layers, which will be named "ROT" hereafter, and 2) an alternation ("ALT") between two fixed directions (commonly – but not necessarily – shifted by 90° between layers along the build direction (BD)) [26].

The ROT strategy is considered to induce the lowest levels of RS, as the 67° angle allows for the maximum number of different directions of the laser scan without repetition, therefore minimizing heat accumulation throughout the added layers [27]. While the influence of scan strategies on RS profiles and magnitudes is the subject of several studies [20,23–28], little is reported about the impact of scan strategy on the cellular microstructure in PBF-LB/M/IN718. Most studies relating scanning strategies and microstructure focus on larger-scale aspects, such as porosity, grain morphology, and texture. For example, Pant et al. investigated the effect of four different scanning strategies on porosity, texture, and residual stress in PBF-LB/M/IN718 [28]. Wan et al. compared samples built with two different scanning strategies (90° interlayer rotations or no interlayer rotations) in terms of grain morphology and texture, attributing the main microstructural differences to heat flux during the building process [29]. Schröder et al. studied three different scanning strategies used within a single PBF-LB/M/IN718 sample, evaluating residual stress and texture, and found the localized transitions between zones built with different scanning strategies to be sharp and well-defined (confined to 100–200 μm) [26].

A few recent works have addressed the characterization of cells in PBF-LB/M materials. Tao et al. provided a thorough characterization of cell morphology and chemistry in PBF-LB/M/IN718 using electron microscopy techniques, including an assessment of cellular spacing, which was reported to be between 0.28 μm and 1.47 μm in that study [30]. Wang et al. investigated the cellular structures in PBF-LB/M/316 L in detail, particularly regarding crystallography and dislocations via electron microscopy, concluding that the cells have a strengthening effect [31]. Likewise, Kikukawa et al. recently reported that the cellular structures increase the yield strength of PBF-LB/M/IN718 by 38 % and can be deliberately utilized to attain superior mechanical properties for advanced applications [9]. Therefore, it is of interest to quantify these microstructural features and to control them via process parameter selection, for example, the scanning strategy. Rielli et al. showed via electron microscopy that two different scanning strategies (chessboard and 90° interlayer rotations) led to differences in cellular spacing in PBF-LB/M/IN718 [32]. Additionally, Serrano-Munoz et al. found contrasting kernel average misorientation values (KAM, linked to local lattice strain due to, *e.g.*, residual stress, high dislocation densities, or segregation) in PBF-LB/M/IN718 samples built with two different scanning strategies, with higher misorientation angles in a sample built with unidirectional scans as opposed to a ROT-type scan [24]. These results suggest that the scanning strategy most certainly has an impact on the cellular structures. Nevertheless, quantification of cell fraction in a statistically relevant manner is lacking. The effect of scanning strategy on the cellular structures is of special relevance for applications that foresee the use of varying scanning strategies, such as repairs [33–35], multi-process AM (*e.g.* combining PBF-LB and DED [5]), or engineering of components with site-specific properties [36–38]. Furthermore, it has been shown that changing process parameters – including the scanning strategy – can enable the design of, for instance, tailored dislocation densities [36] or texture [39].

Regardless of the process parameters, IN718 is a precipitation-hardened alloy which needs to be heat-treated to obtain optimal performance [40]. The heat treatments (HTs) usually consist of stress-relief annealing and/or solutionizing before two-step aging for precipitation of the strengthening $Ni_3(Al,Ti)$ γ' ($L1_2$, *Pm* $\overline{3}$ m) and $Ni_3(Nb,Ti)$ γ'' (DO_{22}, *I4/mmm*) phases [17,41]. The solutionizing aims to dissolve the undesired brittle Laves phase and promote greater chemical homogeneity, while avoiding the formation of the generally detrimental Ni_3Nb δ (DO_a, *Pmmn*) phase [15,22,39,42]. An effective HT for IN718 starts with a successful solution treatment to enhance Nb availability and lay the foundations for optimal γ'' during aging.

HTs for cast or wrought IN718 are well-established, whereas those for the additively manufactured alloy are still under scrutiny [18,42,43], despite the recent publication of an ASTM standard [41]. Different authors give different (sometimes conflicting) recommendations for temperatures and holding times [43–46], often overshooting the temperature and duration of the solution treatment [19], while others skip it completely [47], and a fundamental understanding of the kinetics governing the heat treatment specifically for IN718 processed by PBF-LB, with its particular microstructural characteristics, is lacking. Nevertheless, some general guidelines have proven to be robust. For instance, Gallmeyer et al. suggest that a temperature higher than 1020 °C is sufficient to promote the dissolution of Laves and avoid the formation of δ in PBF-LB/M/IN718 [48]. Additionally, in this system, recrystallization is generally considered to occur above 1100 °C [49]; for example, Karabulut et al. reported widespread recrystallization in PBF-LB/M/IN718 after heat treatment at 1100 °C for 2 h [50].

This study aims to clarify the evolution of the PBF-LB/M/IN718 microstructure during a solution heat treatment, providing insights into the kinetics of dissolution of the Laves phase and the microsegregation associated with the cellular structures. The goal is to monitor the changes in real time and determine time and temperature dependence regarding the elimination of these Nb-rich microstructural features, while avoiding the formation of δ, to enhance Nb availability for precipitation of γ'' during subsequent aging heat treatments. For the purposes of this work, recrystallization is to be avoided, in order to preserve the characteristic cellular aspect of the PBF-LB microstructure, allowing for a process-specific investigation. Moreover, the dislocation structures associated with the cells increase the strength of the material, so their retention can be beneficial [9,10,51]. These constraints set the HT temperature above 1020 °C and below 1100 °C. To complete the investigation, this work also assesses the influence of two scanning strategies (ROT and ALT) on the cellular microstructure, microsegregation, and *in situ* solutionizing behavior of the material. Since different scanning strategies can cause microstructural differences in the material [24], it is important to understand if a specific heat treatment can produce similar effects on ALT and ROT-built samples and bring both to a comparable chemical state, despite the initial differences, while avoiding recrystallization, to be able to take advantage of the cellular structures characteristic of PBF-LB materials.

The tasks at hand would be challenging to fulfill via simulations and would be limited to localized observations and poor statistics using only

electron microscopy. Alternatively, x-ray diffraction (XRD) allows the assessment of the phases present in a sample with greater volume coverage and time efficiency. However, low-energy XRD, as seen in laboratory setups, offers limited time resolution and penetration into the sample, especially in the case of dense materials such as IN718 (approximately 5 μm with a MnK_{α} source [27]). In this context, high-energy synchrotron XRD is a useful technique that allows the identification and quantification of microstructural phases in a bulk sample [52]. Moreover, the higher flux enables the identification of low-fraction phases, such as the Laves phase, and the superior time resolution provides further insights into the diffraction peak shapes, which are relevant when dealing with materials exhibiting segregation and high dislocation densities [20]. By pairing this technique with *in situ* heat treatments, time-resolved insights into the microstructural evolution may be gained [53]. In this case, the *in situ* HT consists of a solution annealing at approximately 1025 °C for 1 h.

A novel approach is introduced to quantify the fraction of cell walls via Rietveld refinement, based on the influence of microsegregation on the lattice parameter. Unlike Williamson-Hall plots or plain Pearson/Voigt deconvolution techniques [54–56], the method presented here is not restricted to crystallite size, lattice parameter, or strain analyses. Instead, it capitalizes on local chemistry variations to discern distinct microstructural features in PBF-LB metals, namely, cell wall and cell core. To the best of the authors' knowledge, this method enabled cell wall fraction quantification in PBF-LB/M/IN718 for the first time. This procedure is then used to compare the two scanning strategies in terms of phase and cell wall contents, and to understand the dynamics of the evolution of cell wall microsegregation during the solution treatment, including *in situ*, online monitoring of the heating stage leading to the isothermal hold, which allows tracking of fast changes happening during the temperature ramp-up. The effect of the heat treatment on ALT- and ROT-built samples is compared and discussed. Due to the experimental restrictions for direct temperature measurement, the temperatures endured by the samples were determined subsequently using dilatometry.

2. Materials & methods

2.1. Sample fabrication

The original samples consisted in two IN718 rectangular prisms of 90 mm (||z) × 20 mm (||x) × 10 mm (||y), and were produced using PBF-LB/M by Materialise GmbH (Bremen, Germany) with their long axis parallel to the building direction (z || BD, *cf.* Fig. 1). One of the prisms was fabricated with a 67° incrementally rotating (*ROT*) scanning strategy, while the other was built with a 0°/67° alternating (*ALT*) scanning strategy (scan tracks parallel to x – 0° – alternating with scan tracks rotated by 67° with respect to x). All samples were fabricated with an EOS M280 system (EOS GmbH, Krailling, Germany), with a layer thickness of 80 μm, using a laser power of 370 W and an energy density of 40.6 J/mm^3. The build job was performed in a controlled argon atmosphere, and the oxygen content in the chamber was kept below 0.2 % by weight during the entire process. No contour scan was used, and the samples were provided in an as-built state. An illustration of the sample geometry and the scanning strategies used is shown in Fig. 1.

The specimens for the synchrotron experiment are small cylinders (1 mm in diameter and 5 mm in length) extracted (by cutting and turning) from the original samples at about ¾ of the height, at the center of the width, with the long axis aligned with the BD.

The chemical composition of the materials was assessed by testing approximately 3 g of material in the form of chips carved out by machining a region of the original prisms at the same height as the synchrotron samples. All metallic elements were measured by x-ray Fluorescence (XRF), except Al, which was quantified by inductively-coupled plasma mass spectrometry (ICP-MS). N and O were quantified via carrier gas hot extraction, and C and S were assessed by combustion analysis. The average chemical composition for each specimen is given in Table 1. No significant difference is observed between the samples.

2.2. In situ synchrotron XRD

2.2.1. Synchrotron XRD experiment

The *in situ* x-ray experiments were conducted at the beamline ID22 of ESRF (European Synchrotron Radiation Facility, Grenoble, France) [57]. The experimental setup can be seen in Fig. 2a and is schematically drawn in Fig. 2b and c. The heat treatments were conducted using the induction furnace depicted in orange in Fig. 2, wherein the specimens were continuously flushed with an argon flow to avoid oxidation. The cylinders, in the as-built condition, were glued at one end of a hollow alumina rod (sample holder, cf. Fig. 2c). The cylinders were then placed horizontally into the furnace (Fig. 2a) so that the beam targets the samples at about ¾ of the sample length (about ½ of the sample length was inserted into the rod).

With the aim of avoiding both δ phase formation and recrystallization, the intended HTs originally consisted of a solution treatment with a heating ramp of 35 °C/min, a hold time of 1 h at 1080 °C, and a cooling rate of 70 °C/min. The solutioning temperature set to the furnace (T_{inp}) was 1100 °C, since the on-site available estimation (cf. Supplementary

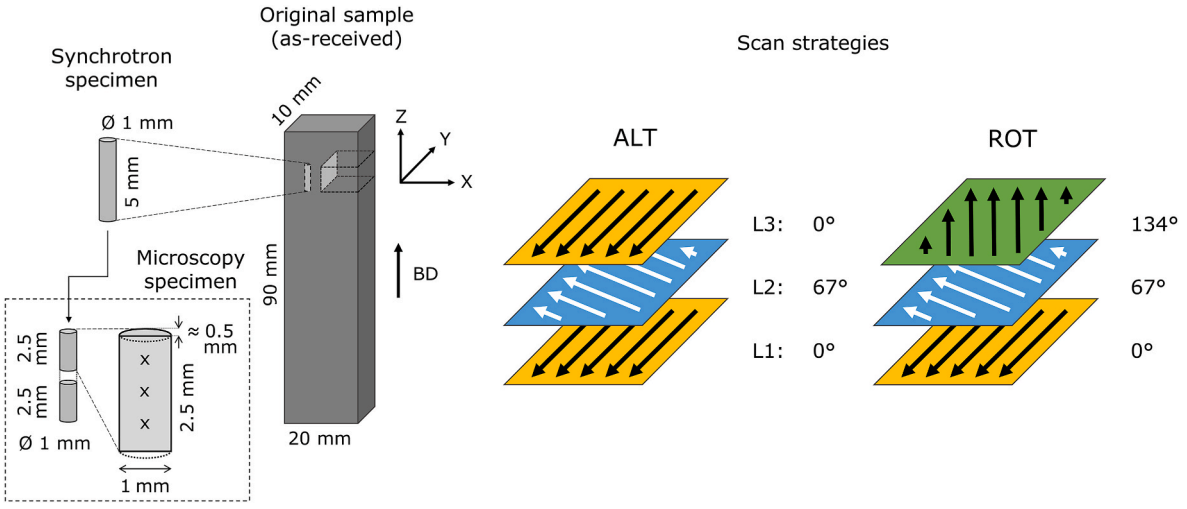

Fig. 1. Schematic drawing illustrating the sample geometry of the original rectangular prisms, in situ synchrotron and ex situ microscopy specimens (left), and scanning strategies (right). The cross marks indicate the approximate locations of the microscopy measurements. For details, see main text.

Table 1
Chemical composition (in weight percentage) of the samples.

	Ni	Cr	Fe	Nb	Mo	Ti	Al	C	O	N	S
ALT	52.3	18.9	18.4	5.20	3.10	0.94	0.421	0.048	0.028	0.013	0.0050
ALT 3σ	0.5	0.1	0.1	0.06	0.05	0.07	0.013	0.002	0.002	0.002	0.0001
ROT	52.2	18.7	18.4	5.13	3.10	0.95	0.423	0.047	0.026	0.014	0.0070
ROT 3σ	0.5	0.1	0.1	0.06	0.05	0.07	0.008	0.002	0.002	0.002	0.0001

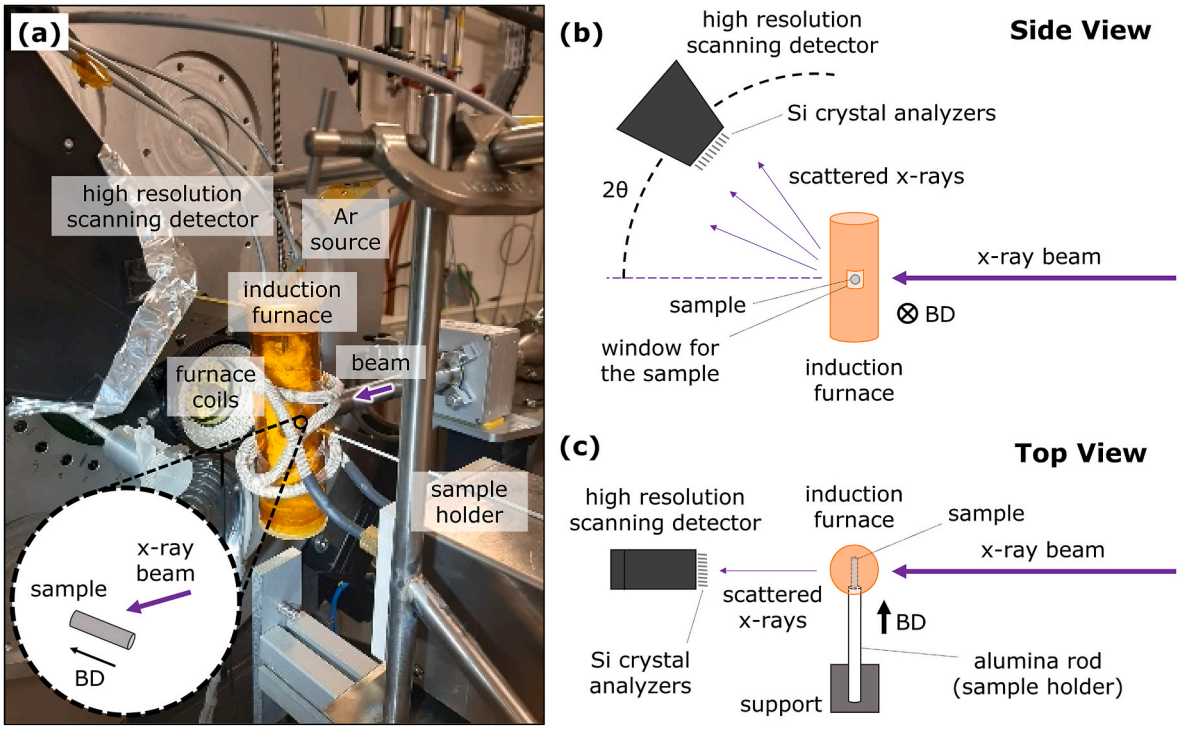

Fig. 2. (a) ID22 experimental setup, with a detail of the specimen and its relative orientation to the beam. (b) Schematic illustration of the experimental setup (side view). (c) Schematic illustration of the experimental setup (top view).

information) of the difference between this and the expected sample temperature (T_{true}') delivered $\Delta T = T_{inp}$ - T_{true}' = −20 °C. Note that this difference was proven much larger after the *in situ* experiments, for which dilatometry was used to better estimate the true dwelling solutionizing temperature T_s (cf. Sections 2.3 and 3.2) experienced by the metal. The heating rate was 36 °C/min, and the cooling rate was 71 °C/min from T_s to approximately T_{true}' = 530 °C, and gradually slower from then on, down to room temperature. The complete temperature profile during cooling is shown in the supplementary information (Fig. S.I. - 1).

Data was acquired at approximately 1.5-min intervals throughout every heating or cooling stage, as well as throughout the isothermal stage of the solution treatment. The energy of the x-ray beam was set to 50 keV, with a wavelength of 0.24802 Å (±0.00001 Å), calibrated using a NIST Si 640c reference. The beam was defined with a cross-section of 1 × 1 mm^2, and the effective 2θ range of acquisition was 0.0°–26.0° (q ranging from 0 to 11.4 $Å^{-1}$). The high-resolution scanning detector (Dectris Eiger 2 X 2M − W CdTe) [57] was used throughout the entire experiment, combined with the Si analyzer crystal array. Although initially planned, it was not possible to use the area detector also available at ID22 (PerkinElmer XRD1611) [57] during this experiment, owing to unforeseen disturbances induced by the electromagnetic fields emanating from the induction furnace.

The direct online measurement of the metal temperature during the experiment was not possible for several reasons. Due to the small size of the samples, spot welding of thermocouples onto the specimens was considered unsuitable, as the high temperatures experienced during welding could have altered the local chemical segregation and microstructure of the material. Moreover, it was not possible to physically attach or wrap the thermocouple in a robust manner that would impede relative movement (due to looseness or thermal expansion) or interaction with the x-ray beam, affecting the diffraction patterns. Lastly, it was not possible to position the sample and the thermocouple simultaneously inside the furnace due to space constraints. Therefore, the experiment was carried out using the furnace calibration (without sample), and the metal temperature was determined afterwards using dilatometry tests to correlate the macroscopic thermal expansion (measured by dilatometry, knowing the exact temperature endured by the specimen) with the thermal expansion calculated with the lattice parameter from the diffraction data. This procedure is further described in section 2.3.

2.2.2. *Synchrotron XRD data analysis*

The diffraction data was initially processed through the software PDIndexer [58] (plotting, peak indexing, and single peak fitting using a split Pseudo-Voigt fit to account for peak asymmetry), and later refined by the Rietveld method with the software TOPAS [59], via CIF files obtained from the Inorganic Crystal Structure Database (ICSD) and from the Crystallography Open Database (COD). The refinement was set up as a simultaneous fitting of the diffraction profiles for both scan strategies (ROT and ALT) for each temperature value, regulated by the Debye-Waller factor. This way, any error in the phase fraction calculations is systematic and equal for both samples. In other words, the trends and general behavior are trustworthy, despite the approximations and assumptions necessary to allow the refinement.

For the Rietveld refinement calculations, a novel approach was applied in which the peak shoulders corresponding to compositional straining at the cell walls (*i.e.* solute atoms expand or compress the matrix lattice) were fitted as if they were a different phase. More specifically, the microsegregation at the cell walls was fitted based on the γ phase (space group Fm $\overline{3}$ m) CIF but with a different chemical composition due to segregation, and therefore a different lattice parameter. The differences between cell wall and cell core also relate in part to the increased dislocation density at the walls and the consideration of local microstresses. Still, the Rietveld-based approach presented here is grounded in the segregation component of the cell walls. The chemical compositions used in the calculations were extracted from STEM-EDS measurements by Godec et al. [5] and are presented in Table 2.

To take into account the effect of local chemical variations, other chemical compositions (obtained via SEM-EDS) were tested as well, both from literature and from measurements on the samples investigated in this study. These alternative compositions include, *e.g.*, Nb contents ranging from 6.9 % to 14.2 % (wt.%) on the cell wall and are summarized in Table S.I. – 1. Since these variations produce only a limited impact on the results of the Rietveld refinements (cf. Table S.I. – 2), the authors opted for the values reported by Godec et al. due to the improved lateral resolution of the STEM-EDS technique over SEM-EDS, considering the length scale of cell walls.

Besides the cell wall pseudo-phase, the calculations include γ Ni-matrix and Laves phases. The Rietveld refinements were limited to the heating phase of the HT, as that proved to be enough to encompass all changes relevant to the scope of this study. Moreover, it is important to note that, during the temperature ramp-up, the temperature is constantly increasing throughout each measurement (ca. 1.5 min). Therefore, the average temperature values for each measurement period were used as the temperature input for the refinements.

While other diffraction-based methods, such as Williamson–Hall plots or Person/Voigt deconvolution, have been used to study peak broadening and asymmetry induced by microstructural heterogeneity [54–56], these approaches are generally limited to a statistical or phenomenological interpretation of diffraction line shapes. For example, Williamson–Hall analysis can separate broadening contributions due to crystallite size and microstrain based on the angular dependence of peak width, but it does not distinguish between chemically distinct regions or different phases. Similarly, conventional Pearson, Voigt or pseudo-Voigt peak fitting may account for overall asymmetry but does not inherently attribute it to physically separate microstructural populations without strong assumptions.

In contrast, the Rietveld analysis on high-resolution synchrotron XRD data developed in this work leverages the effect of microsegregation on the γ lattice parameter to explicitly model two distinct γ populations in the refinements: a Nb-enriched, compositional strain-bearing cell wall region, and a more chemically homogeneous cell interior. By refining two separate lattice parameters and associated peak shapes and intensities, the approach allows the direct quantification of the cell wall fraction, which is not readily accessible through conventional peak-broadening analysis. Moreover, this physically grounded deconvolution provides a direct link between peak asymmetry and elemental microsegregation, rather than attributing peak distortions solely to crystallite size or strain.

Table 2
Chemical composition input from Godec et al. [3] assumed for Rietveld refinements (in wt. %).

	Ni	Fe	Cr	Nb	Mo	Ti	Al
Cell Core	54.6	19.0	17.4	3.9	3.5	0.7	0.3
Cell Wall	52.5	16.9	16.4	8.6	3.9	1.2	0.3

2.3. Dilatometry

The dilatometry specimens – cylinders of 10 mm in length and 4 mm in diameter – were extracted (by wire cutting and turning) from the same original prisms that were used in the production of the synchrotron specimens, at the region immediately below from where the synchrotron specimens were obtained, with the long axis parallel to the building direction. The dilatometer used was a DIL 805 A/D, from TA Instruments (New Castle, USA), with a type-S thermocouple welded onto the sample, and the HTs replicated those applied during the synchrotron experiment: same intended heating rate (35 °C/min) and intended holding temperature (1080 °C) for 1 h were applied. In this case, however, the sample was cooled down rapidly using a Helium flow.

2.4. Electron microscopy

2.4.1. Scanning electron microscopy (SEM)

The as-built samples for scanning electron microscopy were extracted from the original towers at the same height as the synchrotron specimens, using a precision disc saw (Accutom 10, by Struers, Copenhagen, Denmark), in the form of cubes (*cf*. dotted cuboidal region within tower in Fig. 1). The cubes were then embedded in conductive resin (Technotherm 3000, Kulzer GmbH, Hanau, Germany), with the internal surface exposed (X-Z plane, parallel to BD, *cf*. light grey region within dotted cube in Fig. 1). The embedded samples were ground with SiC emery papers P600, P1200, P2500 and P4000, then polished with 3 μm and 1 μm diamond paste, and finally with a colloidal silica (50 nm) suspension.

Electron-backscattered diffraction (EBSD) was performed on a TESCAN Vega 3 (Brno, Czechia) scanning electron microscope (SEM) equipped with an EBSD detector from Oxford Instruments (Abingdon, United Kingdom), model Symmetry S3. The operating conditions for EBSD were 20 kV as the acceleration voltage, 35 mm as the working distance and 3 ms as the exposure time. The samples were tilted by 70°, and for the maps collected at 100× magnification (2.8× 2.1 mm^2) the step size was 5 μm, and for those collected at 1000x (277 × 208 μm^2), the step size was 0.25 μm. The EBSD data was then processed with the MTEX package [60] for the MATLAB software (The MathWorks Inc., Natick, USA), with a misorientation threshold for high-angle grain boundaries set as 10°, as recommended for additively manufactured metals [61]. Grains smaller than 3 pixels were excluded from the analysis, and non-indexed pixels were made to match their nearest neighbor. The data was denoised via a variational spline filter [62] and smoothened via the default Kernel function for 25 iterations. For the calculation of orientation distribution functions, a La Vallée Poussin kernel, a halfwidth of 5° was used.

Additionally, grain average spread (GOS) and kernel average misorientation (KAM) calculations were executed. GOS refers to the mean misorientation among all pixels within a given grain with reference to the average orientation of said grain, and is used as an indication of recrystallization when the value is below 2° [63]. KAM is defined as the local misorientation of a single pixel with reference to the neighboring pixels, and relates to localized lattice strain (and hence to crystallographic defects that generate lattice disturbances) [64]. In this study, the first order neighboring pixels were used for KAM calculations. The use of denoising filters and enhanced Hough resolution as per Serrano-Munoz et al. grants improved angular resolution (down to sub-0.1°), allowing the observation of sub-grain dislocation structures [65].

Electron-channeling contrast imaging (ECCI) was performed on a JEOL JSM-7200 F (JEOL, Ltd., Akishima, Japan) SEM with a field emission gun (FEG), at an acceleration voltage of 30 kV and a working distance of 3.1 mm. ECCI images were used to determine the Laves phase area fraction via thresholding on two equivalent images (108 μm^2) per scanning strategy using the Fiji software package [66]. Characterization of the chemical segregation by means of energy dispersive spectroscopy

(EDS) was carried out on a FEI Quanta 3D FEG (Thermo Fisher Scientific Inc, Waltham, USA) SEM equipped with an EDS detector EDAX Octane Elect SDDs (Gatan, Pleasanton, USA) and operated at 25 kV and a working distance of 10 mm. Additional backscattered electron (BSE--SEM) images were acquired in the same instrument at 25 kV and 5.6 mm of working distance.

2.4.2. Transmission electron microscopy (TEM)

For the TEM investigations, the as-built samples were prepared by cutting ≈500 μm thick slices from the original towers (perpendicularly to BD) and thinning down the slices by equally grinding both sides with SiC emery paper P600 and P1200 until the thickness reached approximately 100 μm. At this point, discs of 3 mm were punched out from the thinned slices, and subsequently further thinned by twin-jet electropolishing on a Tenupol-3 machine from Struers (Copenhagen, Denmark), using an electrolyte prepared with 950 mL of ethanol (96 %), 100 mL of butanol and 50 mL of perchloric acid, at −25 °C and 20 V.

The TEM used in this study is a JEM-2200FS (JEOL ltd., Tokyo, Japan) with a FEG source and an omega-type energy filter. It was operated at 200 kV using energy filtering (EF) with a slit width of 30 eV in conventional TEM (CTEM) mode for the acquisition of selected area diffraction (SAD) patterns, as well as bright field (BF) and dark field (DF) micrographs.

3. Results and discussion

3.1. As-built microstructure

In the as-built condition, the specimens exhibit the typical microstructural features that are characteristic for PBF-LB IN718 [67]. The BSE-SEM images for both ROT and ALT strategies (Fig. 3a–d, respectively) show elongated cellular structures, and EDS maps on the same regions evidence the presence of microsegregation of, *e.g.,* Nb and Mo at the cell walls (*cf.* respectively, Fig. 3b and c for ROT and Fig. 3e and f for ALT). The cellular structures can be analyzed in greater detail by enhancing ECCI (Fig. 3g–j) through alignment of specific crystal orientations with the incoming electron beam. The cell interiors have darker cores and are delimited by brighter regions that correspond to the cell walls. The latter appear brighter due to a higher dislocation density and microsegregation. In addition, Laves particles decorate the cell walls, particularly at cell wall crossings (white arrows).

The SEM results visually suggest a higher density of cell walls in ALT when compared to ROT strategies. To complement this qualitative observation, the linear density of cell walls was calculated from ECCI images (Fig. S.I. - 2), and resulted in 1.27 ± 0.13 μm^{-1} (cell walls per unit length) for the ALT and 0.93 ± 0.13 μm^{-1} for the ROT scanning strategy. Conversely, an average equivalent projected diameter of the cell walls can be calculated from the same dataset, resulting in 0.80 ± 0.08 μm for ALT and 1.08 ± 0.08 μm for ROT. Although these results support the visual observations, no categorical conclusions can be drawn from the ECCI images alone (or calculations based on them) due to the selectivity of the observations. The determination of cell wall area fraction is challenging due to nuances in contrast and the presence of other particles. Moreover, a true equivalent comparison would require both samples to be imaged with the same crystallographic orientation. To overcome these limitations, synchrotron XRD is employed to investigate the bulk in section 3.3.

The Laves phase area fraction was quantified via thresholding on SEM-ECCI micrographs (Fig. S.I. - 3). No significant differences in the average value (2.49 % ± 0.31 % for ALT versus 2.37 % ± 0.44 % for the ROT strategy) are observed, likely due to the highly localized aspect of this method. Indeed, Capek et al. argue that the quantification of Laves phase in PBF-LB/M/IN718 via electron microscopy is challenging due to the small size and low fractions of these particles, suggesting synchrotron XRD as a more adequate strategy [52]. Therefore, the Laves content is more reliably determined based on the synchrotron XRD data in section 3.3.

A selected region of Fig. 3g is presented at higher magnification in Fig. 3h, where exemplary cell wall borders are marked in yellow dashed lines. The dislocations tend to pile up at cell walls during the PBF-LB processing and subsequent cooling, so an increased amount of dislocations can be observed inside the cell wall when compared to the cell core [68,69]. Black round oxide particles (usually aluminum- and titanium-rich oxides [70,71]) also commonly (but not exclusively) sit at the cell walls (black arrow). Lastly, Nb-rich MC carbides are also present, indicated by a red arrow. These carbides, widely reported in literature [16,72,73], are recognizable by their blocky morphology with straight edges [74].

Fig. 4 presents EBSD orientation maps (IPF Y, XZ plane – parallel to BD) and pole figures for both specimens in the as-built state. The pole figures indicate a weak <110> || BD texture and no significant difference between them at this scale: maximum 1.9 MRD (multiples of random distribution) for ROT and 1.8 for ALT (as compared to values upwards of 4 MRD commonly reported in the literature [18,20,69]). In addition, there is an also weak <111> ||Y and X texture component. Interestingly, our ALT strategy (0° + 67°) lead to lower MRD levels than the 0° + 90° alternating scanning usually reported in the literature (see for *e.g.* refs. [27,29]). The slight rotation of the ROT pole figures along Y (compared to ALT) is most likely an artifact due to sample mounting in the microscope. There is no significant difference in terms of grain size either, with a mean grain size (equivalent diameter) of 51 μm ± 34 μm for ROT (from 9021 grains in the map) and 48 μm ± 29 for ALT (from 9248 grains).

3.2. Determination of temperature by dilatometry

From the macroscopic length change of dilatometry data, the thermal expansion, *Exp*, was calculated according to $Exp = (L_t - L_0)/L_0$, where L_t is the current length at any given time, and L_0 is the initial length at room temperature [75]. At the same time, the thermal expansion can also be calculated from the lattice parameter evolution of the γ matrix from the diffraction data, *i.e.*, $Exp = (a_t - a_0)/a_0$, where a_t is the lattice parameter at any given time during the experiment, and a_0 is the initial lattice parameter at room temperature [76]. In the latter expression, the γ matrix is assumed to induce all of the thermal expansion or, *id.*, the thermal expansion of the whole material equals the lattice expansion of the matrix. The validity of this assumption was justified by also considering the expansion of the Laves phase via the rule of mixtures and noting that the change in the Exp was insignificant, which goes hand-in-hand with the fact that the matrix represents more than 95 % of the total (in weight percentage).

The curves for thermal expansion *vs.* temperature using both techniques are plotted and fitted in Fig. 5. The region of interest lies above 600 °C, below which the furnace used at the synchrotron was not calibrated, and below 800 °C, above which other phenomena such as dissolution of microsegregates significantly start taking place and additionally affecting the lattice parameter behavior. Using the fitted expressions for the curves in this region, for a certain value of *Exp*, *e.g.* 1 %, the values of temperature at which the expansion happens are determined for each technique. For example, in the case of the *ROT* specimen, for 1 % thermal expansion, the diffraction method gives 747 °C, while dilatometry gives 673 °C (cf. Fig. 5a). Since dilatometry is the reference method, 673 °C is considered the correct temperature for this thermal expansion. Therefore, it is established that there is a 74 °C difference between the actual metal temperature on the specimens during the *in situ* synchrotron experiments and the nominal input temperature of the furnace.

This procedure was also performed for thermal expansions of 0.9 % and 1.1 %, and the average number among the three results (73 °C) was taken as the final offset. This whole procedure was repeated for the *ALT* specimen, and the result was established to be a 74 °C difference. Hence, the holding temperature for the *ROT* specimen is 1100 °C–73 °C =

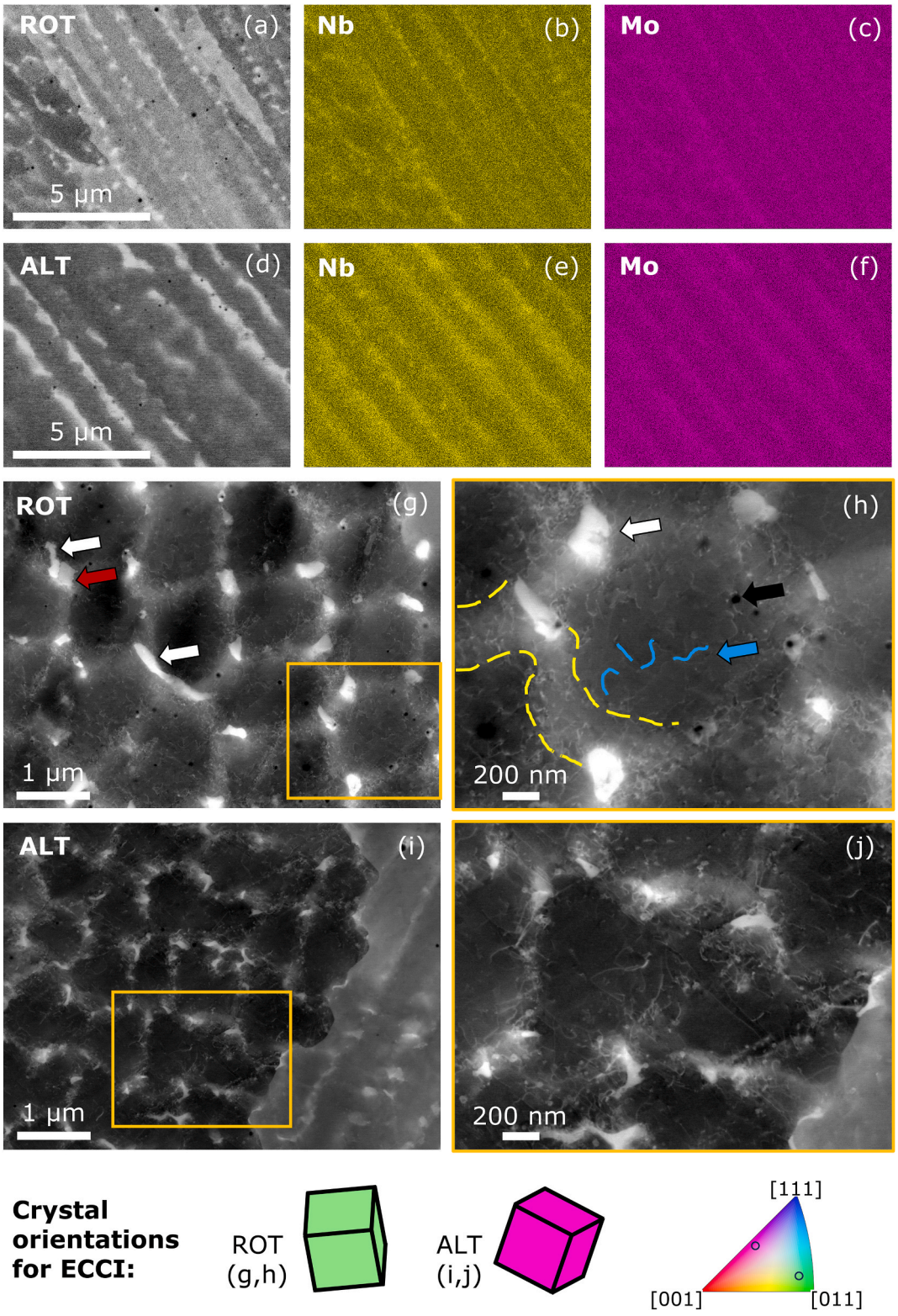

Fig. 3. Representative SEM-BSE image (a) of the ROT specimen with corresponding EDS maps showing the intercellular segregation of Nb (b) and (c) of Mo. (d) SEM-BSE image of the ALT specimen and corresponding EDS maps showing the (e) Nb and (f) Mo segregation. (g,i) Respective ECCI images of the ROT and ALT specimens, with arrows indicating Laves particles (white) and MC carbides (red). (h,j) Higher magnification details of (g,i), respectively, with yellow dashed lines highlighting the cell wall, blue lines illustrating dislocations, and arrows indicating Laves particles (white), oxides (black), and dislocations (blue). The specific crystallographic orientations of the grains shown in (h) and (j) are illustrated at the bottom of the figure, with the corresponding IPF coloring (see black circles on IPF triangle).

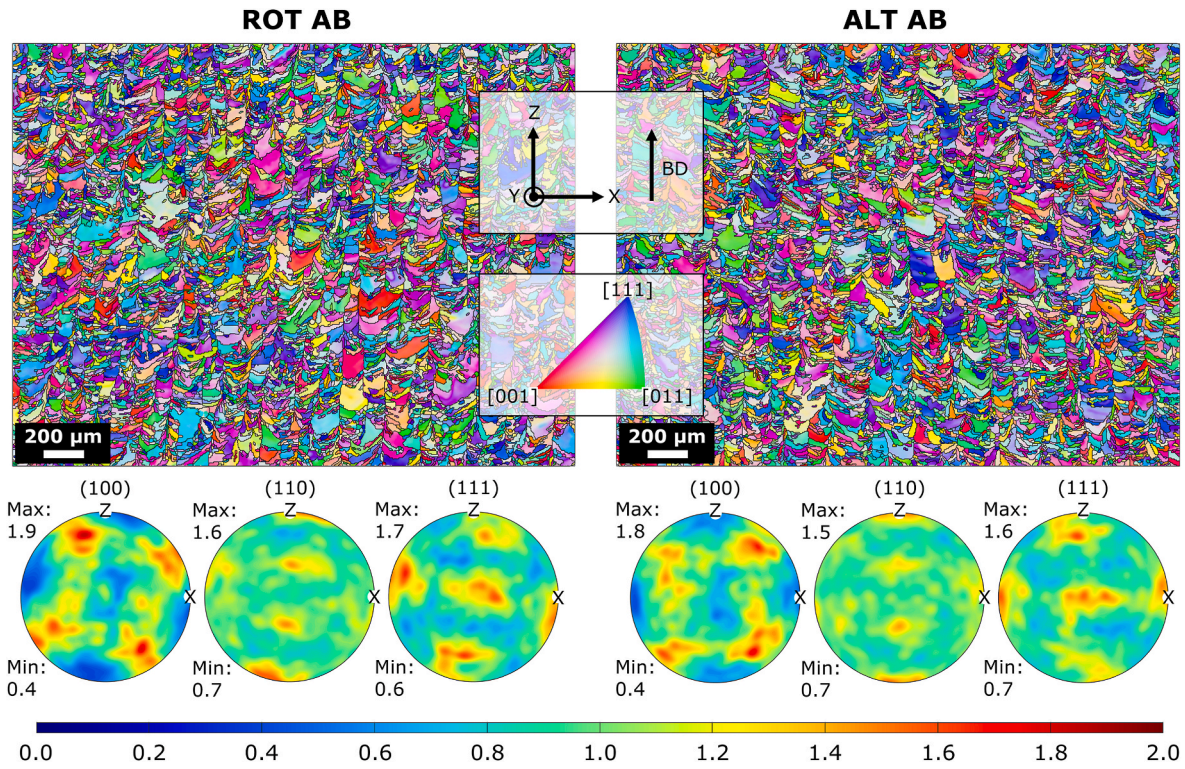

Fig. 4. EBSD IPF Y maps (top) and corresponding pole figures for both ROT and ALT specimens.

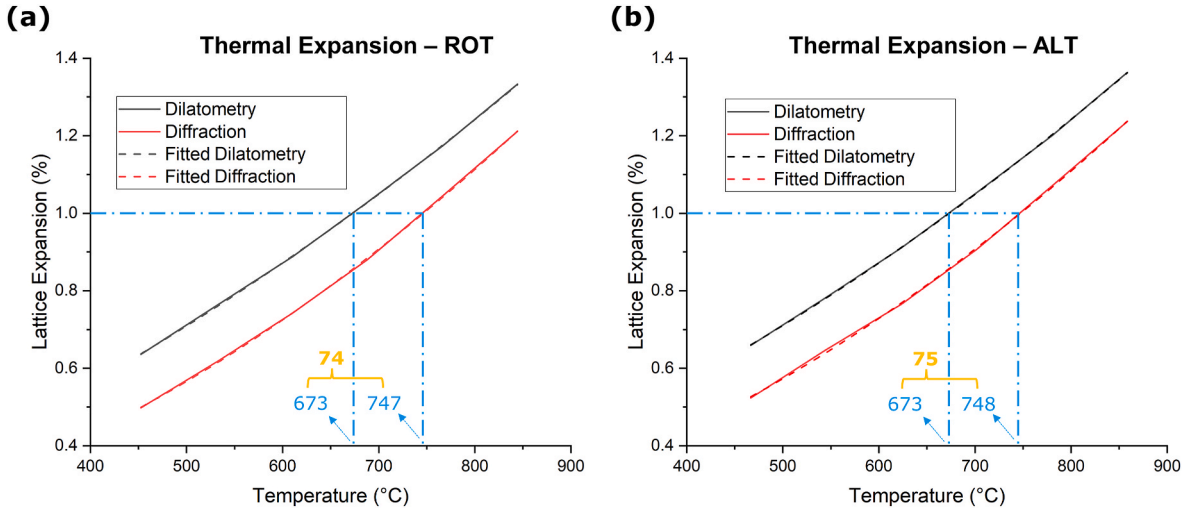

Fig. 5. Plots comparing the thermal expansion calculated from the dilatometry (in black) and from the diffraction data (in red) for each specimen. (a) ROT (b) ALT.

1027 °C. Analogously, for the ALT specimen, it is 1026 °C. These temperatures are consistent among the samples and are still above the δ-solvus (1010 °C [77]), and above the recommended temperature of 1020 °C by Gallmeyer et al. [48] to achieve Laves phase dissolution. Therefore, the objectives of the investigation were not affected. A summary of these conclusions is presented in Table 3.

Table 3
Summarized results of the effective temperature assessment via dilatometry. "Temperature Difference" stands for the difference between the input value and the temperature on the sample.

Sample	Furnace Input Temperature (°C)	Temperature Difference (°C)	Effective Sample Temperature (°C)
ROT	1100	73	1027
ALT	1100	74	1026

3.3. Time-resolved synchrotron x-ray diffraction

3.3.1. As-built condition

The experimental and fitted diffraction profiles (as explained in Section 2.2) for the ROT specimen in the as-built condition are reported in Fig. 6a. The results of the fit for the ALT specimen are similar, as shown in the supplementary information (Fig. S.I. - 2), together with a zoom on the region indicated in Fig. 6a for ROT. The fit is overall satisfactory (see "Difference" profile in cyan), with a goodness of fit of 2.4 for the as-built condition at room temperature (calculated according to ref. [78]), thanks to the weak crystallographic texture, allowing for

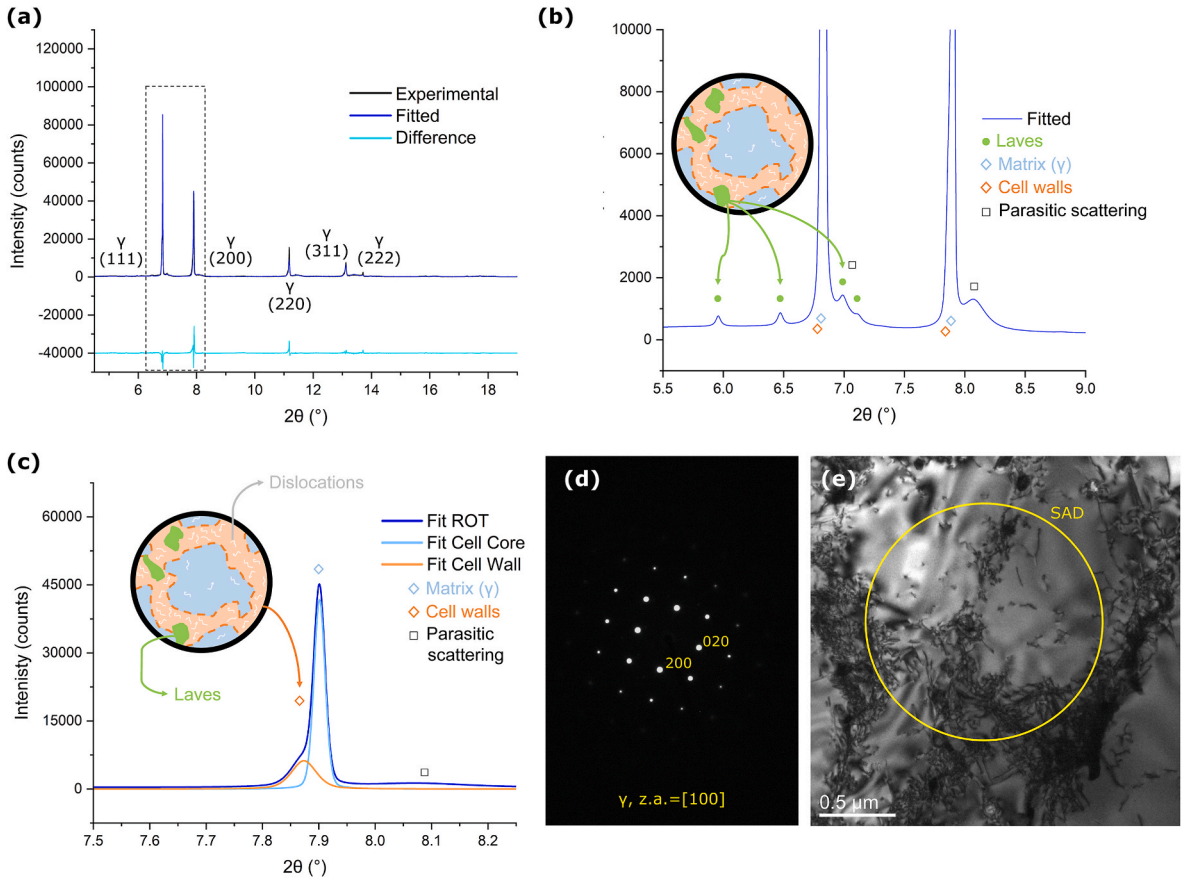

Fig. 6. (a) Experimental and fitted diffraction profiles for the ROT specimen in the as-built condition; an enlargement of the dotted region can be found in Fig. S.I. - 4. (b) Detail of the fitted profile between 5.5° and 9.0°. Laves peaks indicated and an ECCI inset highlights Laves particles. (c) Detail of the fitted γ (200) profile between 7.5° and 8.3°. Inset shows ECCI micrograph correlating the peak asymmetry to the cell walls. (d) SAD pattern along [001] zone axis (z.a.) from yellow circle in (e) CTEM micrograph of ROT, including cells and cell walls. Only the characteristic pattern for γ is seen.

quantitative analyses via Rietveld refinements. Laves peaks in the as-built state occur at approximately 2θ = 5.9, 6.5, 6.9, and 7.1° (Fig. 6b). There is an asymmetry in the form of a shoulder to the left of the peak center for all γ peaks. Exemplarily, the asymmetric nature of γ (200) is clearly observed in its 2θ enlargement in Fig. 6c.

Some authors have affirmed that this asymmetry is due to the presence of γ'' particles [20,44,52,79]. Nevertheless, several other studies report the absence of γ'' in as-built AM IN718 [18,45,80,81]. Our TEM investigations also confirm the lack of γ'', as shown by the absence of its characteristic reflections and streaks on the [001] SAD pattern (Fig. 6d) from the region marked with a yellow circle on the BF-CTEM in Fig. 6e. It is therefore considered that the presence of Nb and Mo atoms in solid solution at the cell wall can locally increase the lattice parameter, bringing their contribution to the diffraction peak slightly towards lower values of 2θ, thus creating the asymmetry. In fact, Schröder et al. recently hypothesized that the contribution of the cell walls to the γ-Ni diffraction peak (corresponding to the interior of the cell) can be described as an asymmetric tail (in 2θ or Q) left of the γ peaks [81].

Note that "bumps" (low and broad peaks) are present on the profiles to the right of every γ peak. This effect is a consequence of parasitic scattering (scattering that goes directly to the detector, bypassing the Si analyzer due to its low diffraction angle) [82], due to the high energy (50 keV) used in the measurements. In fact, these bumps appear and are noticeable only in the vicinity of the high-intensity peaks. Moreover, the attribution of such bumps to parasitic scattering is further corroborated by the fact that these bumps are present and remain practically unchanged in all profiles, regardless of the temperature or heat treatment time, and for all specimens. This indicates that they do not correspond to a microstructural feature, but rather an experimental artifact. To further validate this interpretation, additional measurements at lower energies (35 keV) were conducted after the original experiment (50 keV). As expected, the bumps were not present in the additional dataset, due to the lower energy (and thus penetration) of the x-ray beam. Therefore, this confirms the artifactual nature of such bumps. The diffraction profiles from this second set of measurements executed at lower energy are reported in the supplementary information (Fig. S.I. - 3). Upon data processing, the bumps associated with parasitic scattering were then fitted and included as part of the background, to not interfere with phase quantification. Since these bumps follow the same periodicity as the γ peaks in the diffraction profile, their fitting was performed using an initial CIF file of pure Nickel, exploiting the good correspondence regarding peak positions. Because the bumps were fitted and included in the background, they did not affect the phase quantification procedure.

A comparison between the diffraction profiles for the two as-built specimens (Fig. 7) reveals some differences between the two scanning strategies, otherwise not observable via SEM-EBSD. First, a slight difference in terms of texture is observed: the γ (111) peak in the ALT specimen is proportionally more intense (relative to the other γ peaks) when compared to that of the ROT specimen. This was expected and is in agreement with literature, since the 67° rotational scans are known to reduce texture [1]. The discrepancy regarding the EBSD measurements could be related to the probed volume and number of grains, local variations, or relative specimen rotation or tilt during the experiments. Note that for the purposes of Rietveld refinement, the texture is assumed to be the same for both scanning strategies.

Second, the analysis of the diffraction data via Rietveld refinements indicates that the ALT specimen contains a higher weight percentage of cell walls than the ROT specimen: 23.7 % ± 0.6 % in ALT, versus 18.5 %

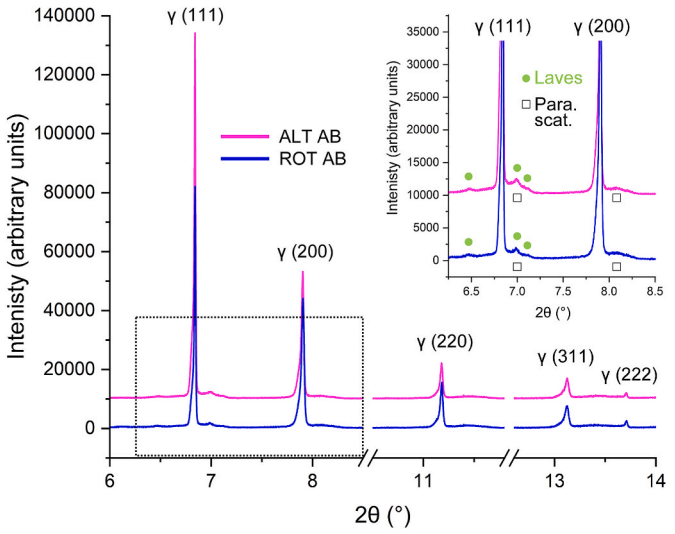

Fig. 7. Fitted XRD profiles for ROT (blue) and ALT (pink) in the as-built condition. The inset shows details for the (111)/(200) γ peak vicinity in the doted box including indexed Laves peaks.

± 0.6 % in ROT, resulting in a difference of approximately 5 % between the two scanning strategies. Furthermore, the calculated fractions (weight percentage) of Laves in ALT and ROT specimens via Rietveld refinements are 1.3 % ± 0.1 % and 1.1 % ± 0.1 % respectively. The latter results align with the findings of Rielli et al., who observed that different scanning strategies, namely *chessboard* (distributed square islands) versus *meander* (similar to ALT but with 90° rotations instead of 67°) led to different Laves volume fractions (respectively 1.9 % and 0.9 %) in as-built PBF-LB/M/IN718 due to differences in thermal history [32].

These results also corroborate what was visually and qualitatively inferred from the SEM (ECCI and EDS) investigations (Fig. 3), which suggested a higher density of cell walls (on equal areas) in the ALT sample, although that method is limited to localized observations. The SEM observations also showed that the cell walls host most Laves phase particles. Since the fraction of cell walls differs between the scanning strategies, one could expect the Laves content to differ as well. These differences between the two scanning strategies regarding the cell walls and Laves phase fractions can be traced back to the differences in heat flow and cooling rates defined by the two different scanning strategies. The ALT scan, by repeating the same scanning pattern more often than ROT, causes a more uneven heat distribution and enhanced differential cooling, which can explain the increased cell wall density and the associated microsegregation and Laves phase contents. This discussion is deepened in section 3.4, upon post-mortem SEM investigations.

To consider the local variations in the chemistry of cells cores and cell walls, further calculations were performed using additional chemical compositions as input. These compositions are presented in Table S.I. – 1, and the results of the Rietveld refinements using those compositions are summarized in Table S.I. – 2 for the as-built condition. The effect of the varying chemistry on the fraction of cell walls and Laves phase is limited to differences below 1 %, with the cell wall fraction ranging from 24.0 % ± 0.7 %–24.7 % ± 0.7 % in ALT and from 18.7 % ± 0.6 %–19.3 % ± 0.6 % in ROT (wt.%). Therefore, the relative difference of approximately 5 % between ALT and ROT is maintained. The Laves content stays between 1.5 % ± 0.1 % and 1.6 % ± 0.2 % for ALT and between 1.2 ± 0.1 % and 1.3 ± 0.1 % for ROT. The modest effect of local chemistry variations on the cell wall and Laves contents is explained by the fact that in highly-symmetric γ or hcp phases, the Rietveld refinements ultimately rely on the average electron density of each phase, which diminishes the impact of slight local differences in chemistry.

3.3.2. *In situ heat treatment*

During the temperature ramp-up, the diffraction profiles shift towards lower 2θ values due to the thermal expansion of the lattice parameter. This effect is shown in Fig. 8a for the γ (200) peak of the ROT specimen. The same shifting behavior is also observed for the ALT specimen and reported in the literature (see for *e.g.* ref. [83]). More importantly, between 811 °C and 889 °C, the peak asymmetry vanishes and the γ peaks become symmetric. This is indicative of the dissolution of the cell walls already during the late phase of the temperature ramp-up, before reaching the isothermal stage of the heat treatment. This dissolution is related to both an elemental homogenization (conversely to observations by Schneiderman in *situ* synchrotron XRD measurements during solidification of high-entropy alloys [56]) and a partial recovery (reduction of dislocation density [84,85]). The goodness of fit remains satisfactory and, in fact, improves at higher temperatures (*e.g.*, 2.1 for ROT at 648 °C).

The Rietveld refinements (Fig. 8b) indicate that the fraction corresponding to the cell wall peak is originally (AB state) higher for the ALT

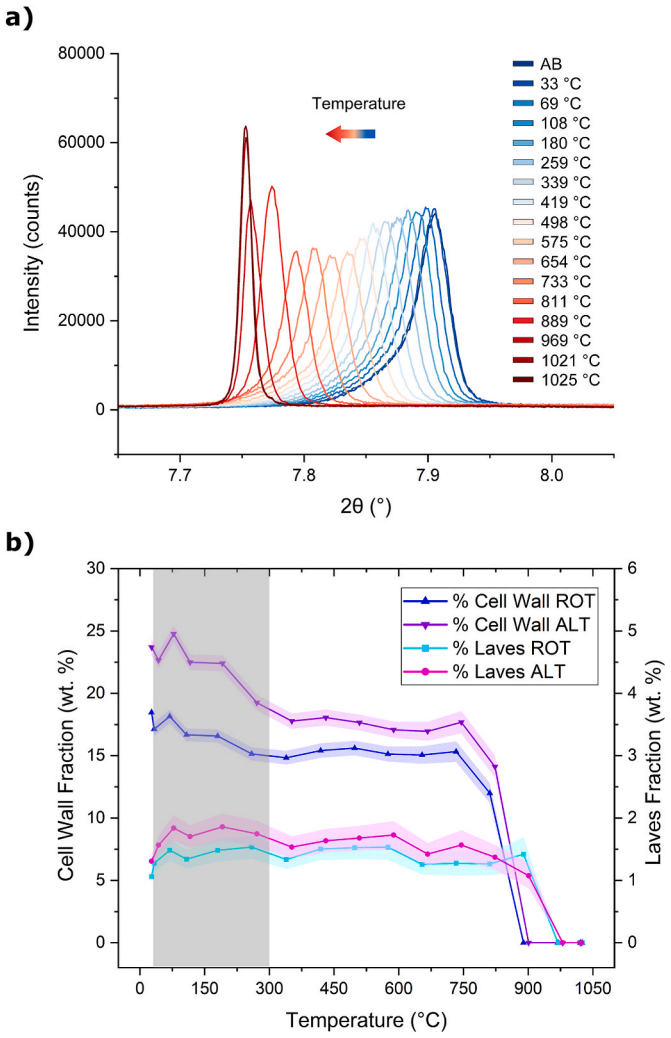

Fig. 8. (a) Evolution of the (200) γ Ni peak of the ROT specimen during the ramping up to the holding temperature. The arrow indicates the temperature increase. (b) Constituent fraction evolution during the ramping up calculated via Rietveld refinements for the two scanning strategies, in weight percentage. The cell wall fraction is read on the left axis, and the Laves content on the right axis. The grey region comprising the three points following the initial point at room temperature denotes an interval of increased data scattering due to inhomogeneous temperature throughout the sample during the first moments of heating.

strategy (ca. 24 % against ca. 19 %, weight percentage). The fraction of cell walls decreases gradually (steeper in the case of the ALT specimen) as the temperature increases, until approximately 400 °C. Then, it remains approximately constant until about 750 °C. It is unlikely that any diffusion-based phenomena take place in this temperature range, so the gradual decrease seen until 400 °C can be an artifact stemming from the fitting or other contributions to peak size. For example, it is possible that the cell wall peak gets obscured by the main γ peak due to different coefficients of thermal expansion, as a consequence of the locally different chemistry owing to microsegregation. Nevertheless, from 750 °C, the fraction of cell walls decreases rapidly, reaching zero just before 900 °C for the two scanning strategies.

The Laves weight fraction, on the other hand, remains practically unchanged until 800–900 °C, where it starts decreasing, reaching zero just below 1000 °C. Since the Laves particles are predominantly found at the cell walls, their dissolution can be closely linked to further changes in the cell walls, corroborating the elimination of microsegregation. Multiple authors [13,15,47,72,86] have reported on Laves particles still remaining in PBF-LB/M/IN718 after heat treatments that were performed at temperatures as high as 1080 °C for 1 h [13]. It is possible, therefore, that some small and sparsely distributed particles could still remain in our specimens, as shown in refs. [13,72], but their fraction at 1027 °C is below the XRD detection threshold (i.e., below ~1 % volume fraction).

Another phase present in the material at every step of the HT is Nb-rich MC-type carbides. These carbides, widely reported in the literature, are a primary phase known to form during solidification at higher temperatures, and they sit mostly at grain boundaries [16,71,72]. The MC carbides were not included in the final Rietveld calculations, as their fraction is not expected to change in the studied temperature range. In addition, simplified, preliminary calculations including MC carbides showed no variation in their weight fraction. Hence, they were removed from the final calculations to make the refinements computationally lighter and less constrained. It is important to note that the first few points after the initial room-temperature point (marked within the grey rectangle in Fig. 8b) exhibit an increased scatter due to inhomogeneous

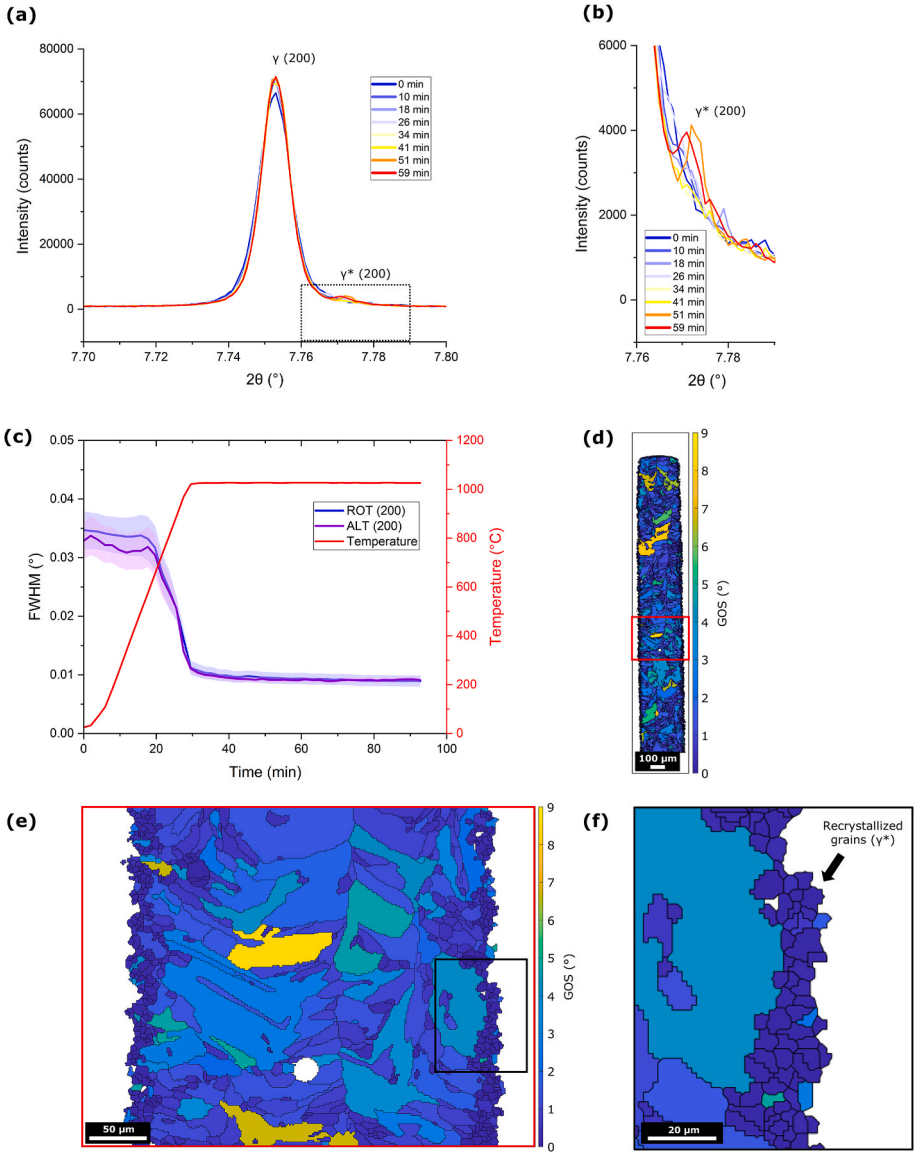

Fig. 9. (a) Evolution of the matrix's (200) diffraction peak during the isothermal stage of the heat treatment. γ* denotes the recrystallized peak emerging during the heat treatment. (b) Detail of the recrystallized γ* peak shown in (a). (c) Evolution of the full width at half maximum (FWHM) of the γ (200) peak during the ramping up and holding stages calculated using PDIndexer. (d) Grain average spread (GOS) map of the ROT specimen after heat treatment. (e) Higher magnification detail of the GOS map: the recrystallized grains lie predominantly on the outer edges of the specimen. (f) Detail of a region surrounding the surface of the sample, as indicated by black box in (e).

temperatures in the sample and possibly unstable output temperatures from the furnace in the first moments of heating.

At 1027 °C, as the isothermal hold progresses, the diffraction peak width decreases marginally due to recovery. This is shown visually through the peak shape in Fig. 9a, and confirmed in Fig. 9c via the evolution of the full width at half maximum (FWHM) as a function of time. After reaching the isothermal stage, although more discrete, a further decrease in the FWHM is observed between the 30 and 40-min mark (the first 10 min of isothermal hold). After that, the decrease in the FWHM is hardly noticeable. These findings corroborate those of Gallmeyer et al. [48], suggesting that a 15-min hold at 1020 °C is enough to induce the desired microstructural homogenization, granted the temperature is uniform in the sample, which might not be the case for big industrial parts. The consideration that microstructural changes happen at a faster rate in additively manufactured nickel alloys compared to the conventionally processed materials has been reported by several authors [11,47,48]. The reasons for this behavior include the short diffusion distances created by the cellular microstructure, and enhanced diffusivity due to the high dislocation densities and high of grain boundary density compared to cast materials [3,10].

It must be noted that another peak, denoted γ*, forms and grows marginally to the right of the γ (200) peak during the hold time at 1027 °C (in Fig. 9a and b). This new peak does not correspond to a new phase, and thus, we attribute it to localized recrystallization. Although recrystallization takes place above 1100 °C in PBF-LB/IN718 [49,50], the occurrence of recrystallization in this case was most likely induced by electrical discharge machining, which was used to prepare the synchrotron specimens. Recrystallized grains can be recognized by GOS values close to zero [63,87,88], so a GOS map was obtained from the EBSD data (Fig. 9d and e). Indeed, the GOS map shows a high concentration of small equiaxed grains with near-zero GOS values towards the surface of the sample, indicating the occurrence of recrystallization within a 10–20 μm layer from the free surface of the specimen (Fig. 9f).

In addition to this, the specimen oxidized during the heat treatment. Since oxidation was also limited to the surface, it coincides with the areas affected by recrystallization. The co-occurrence of oxidation and recrystallization may explain the shift of the γ* peak to slighter higher 2θ angles relative to the main γ peaks, owing to the locally altered chemistry, *i.e.*, the oxygen in solid solution, combined with a local Cr depletion, leads to a lower lattice parameter in the recrystallized γ* grains affected by nearby oxidation [89–91].

The samples were also aged (*in situ*, at 710 °C for 5 h) after the *in situ* solution treatment, before being prepared for *ex situ, post mortem* SEM, as part of a follow-up study. Nevertheless, the aging heat treatment is not expected to significantly influence the EBSD/GOS measurements or the occurrence of recrystallization, due to the lower temperature regime. As a matter of fact, the changes produced by aging at 710 °C (formation of nanoscale strengthening precipitates) are not visible via SEM methods due to their reduced length scale, below the resolution limit of these techniques [32,48]. Moreover, the occurrence of recrystallization in this system is not observed until hundreds of degrees above this temperature, usually above 1100 °C [48,49].

3.3.3. Solutionized condition

Due to the rapid cooling (71 °C/min from the solutionizing temperature – 1027 °C – to approximately 530 °C, or 52 °C/min down to approximately 350 °C), no meaningful microstructural changes happened after the isothermal stage. In other words, the cooling rates used in the experiment did not allow sufficient time for precipitation of other phases, *e.g.*, notably δ. This is in line with other studies and general recommendations for this alloy. For instance, Kouraytem et al. [49] reported that a cooling rate of 10.4 °C/min (from 1250 °C) is enough to avoid the formation of δ (with only limited presence at one out of 30 investigated grain boundaries). Moreover, Pereira et al. [86] suggest that a homogenization HT at 1093 °C must be followed by cooling from 1093 °C to 482 °C in under 45 min (resulting in a minimum cooling rate of 13.6 °C/min) to prevent precipitation of other phases. The cooling rate applied in the present study surpasses all those values, so no precipitation is to be expected.

The solution HT does not seem to alter the texture, since the γ-peak proportions are maintained (Fig. 10). Due to the reduced size of the samples, a clear and reliable texture assessment by means of EBSD is not possible. Nevertheless, the Laves peaks disappeared after the solution treatment, indicating a successful solubilization of the Laves phase (see Fig. S.I. - 4), at least within the detection limits of synchrotron XRD.

3.4. Solutionized microstructure

The SEM analysis of the heat-treated specimens confirms the removal of microsegregation (via EDS, see Fig. S.I. - 5 b,c,e,f) and the persistence of cellular structures within the grains after HT for 1 h at 1027 °C (via SEM-BSD and EBSD-KAM, respectively Fig. S.I. - 5a,d and Fig. 11a–d). In Fig. 11a–d, the color-coded maps represent spatially resolved KAM variations below 0.4° within grains with their high-angle grain boundaries (HAGBs >10°) in black. While all the maps look similar, the KAM cumulative distribution in Fig. 11e confirms that the ALT specimen exhibits higher KAM angles in the as-built condition than the corresponding ROT specimen. All the curves converge towards ≈0.9 fraction of cumulative probability capped at 0.4°, so that only a small fraction of KAM values is expected to be found within the 0.4°–10.0° range. A clear trend within all maps is the long straight alignment of discrete parallel lines, often aligning parallel to straight LAGBs. This geometry matches that seen in SEM-BSE images of the cells that are contained in the sample plane (*cf.* Fig. 3a–d and Fig. SI. - 5a,d), whence these probably represent cell boundaries, which are also known to present misorientations in this angular range (<0.4°).

In fact, Serrano-Munoz et al. used an analogous KAM-based technique to observe intragranular dislocation structures in wrought commercially pure aluminum after creep [65]. In a similar fashion, Deng et al. employed KAM-based analyses to study localized residual stress and dislocation densities in PBF-LB/M/IN718 [69]. Granted EBSD-KAM can only map the effects of geometrically necessary, and not of statistically distributed dislocations (GNDs and SSDs, respectively), the cumulative KAM probability in Fig. 11e shows a measurable larger-angle KAM with a wider spread in the AB ALT specimen than in its ROT counterpart. The two heat-treated conditions exhibit similar KAM angle distributions towards further lower angles than both AB conditions, indicating that there is a threshold for recovery at most at 1027 °C, regardless of the starting dislocation content in the present AB conditions. More specifically, the shift towards lower KAM values indicates

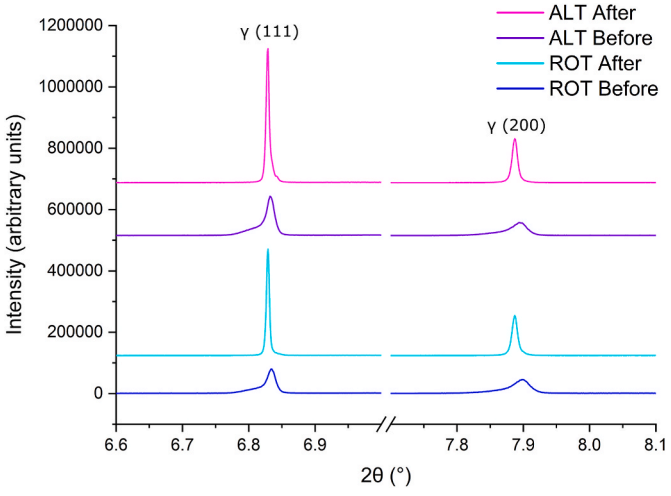

Fig. 10. Synchrotron XRD profiles of the ROT and ALT specimens before and after heat treatment.

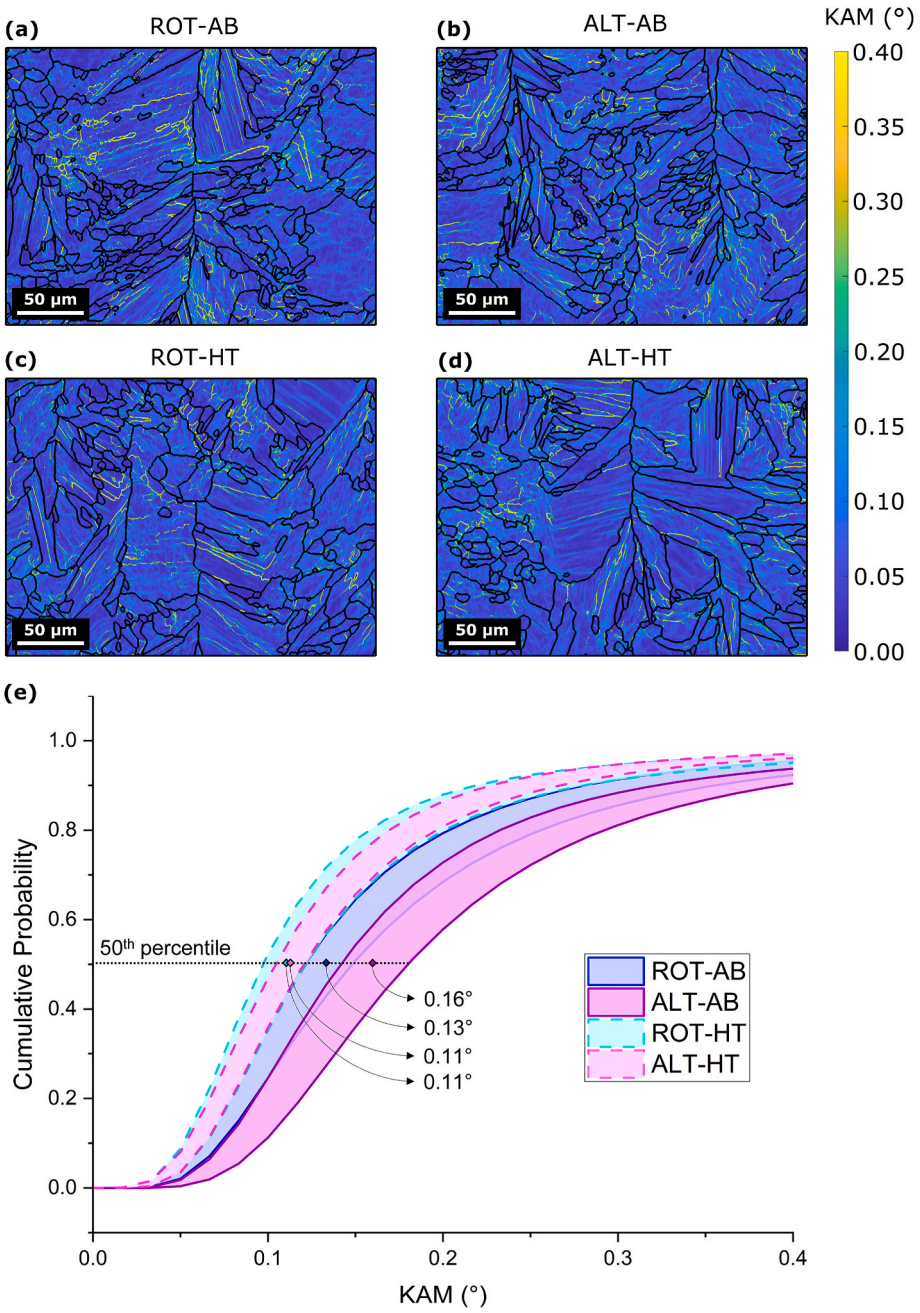

Fig. 11. KAM calculation from EBSD measurements for (a) as-built ROT, (b) as-built ALT, (c) heat-treated ROT, and (d) heat-treated ALT. (e) Cumulative probability plot against the KAM angle distribution of all conditions. For each condition, three measurements were made at three different locations. The bands indicate the spread among those three KAM maps of each condition. The 50th percentile at the midpoint of each band is indicated and labeled.

recovery occurs more in the form of annihilation and less as polygonization of dislocations, as the latter would increase and not reduce KAM angles. In other words, the KAM values for ALT and ROT are different in the as-built condition, but are brought to equivalent levels after the heat treatment. Exemplarily, the 50th percentile for each condition (taken as the midpoint within the bands in Fig. 11e) is 0.16° for ALT and 0.13° for ROT in the as-built condition, and 0.11° for both ALT and ROT after the heat treatment.

These findings can be rationalized together with those regarding cell boundary density in sections 3.3.1 and 3.3.2 in terms of the effects of the scanning strategy, which is known to affect the heat flow in the part [20], which in turn impacts many microstructural, chemical, and physical characteristics of the built material. More specifically, the incremental 67° rotation between each layer, as used in ROT, maximizes the number of differently scanned layers (360, to be exact) before repeating the same initial direction of the laser scans. That is the main reason why this particular scanning strategy produces reduced texture and more randomly oriented grains (*cf.* section 3.1). Additionally, this also means that the expected heat is more evenly distributed throughout the volume of the part, which could benefit diffusion of atoms and limit segregation.

Conversely, the alternation between two fixed laser paths (0° and 67°), as in ALT, means that every two layers, the laser follows exactly the same path, leading to greater heat accumulation and enhancing differential cooling, giving birth to higher degrees of residual stress, higher dislocation density, and more pronounced segregation [92]. These observations are supported by a recent study by Wang et al., who demonstrate that each thermal cycle boosts dislocation density and

incrementally contributes to establish the resulting cellular structures [31]. These results also align with the findings recently reported by Deng et al., which state that increased laser power and decreased scanning speed ultimately lead to higher KAM values, residual stress, and dislocation densities [69].

As aforementioned, the samples were also aged (*in situ*, at 710 °C for 5 h) after the *in situ* solution treatment, before being prepared for *ex situ, post mortem* SEM, as part of a follow-up study. Still, the aging heat treatment is not expected to significantly alter the EBSD/KAM measurements or the microstructure at the scale assessed by SEM. In fact, the observation of the nanoscale products of aging requires the use of higher-resolution techniques, such as atom probe tomography or transmission electron microscopy [32,48]. In addition, this temperature regime does not foresee significant changes in dislocation density in these kinds of alloys either, as attested by Dubiel et al. [93], who reported no significant change in dislocation density in PBF-LB/M/IN625 after aging at 700 °C for 5 h. This aging treatment also does not affect residual stress in this material, as Deng et al. reported no meaningful change in residual stress in PBF-LB/M/IN718 after direct aging (8 h at 720 °C plus 8 h at 620 °C) when compared to the as-built condition [13]. Therefore, the KAM measurements after ageing are considered representative of the strain state after solutionizing. Furthermore, the HT is the same for both scanning strategies, so the comparative aim of this analysis remains valid.

Ultimately, the results offer a new methodology to quantitatively characterize microstructural features relevant to additively manufactured IN718, providing insights to inform heat treatment design for this class of materials in the future. In addition, the present work indicates that most of the significant microstructural changes happen during the heating stage of this solution treatment: removal of microsegregation, minimization of Laves content, prevention of δ formation, and preservation of the cellular nature of the microstructure. The HT at 1027 °C for 1 h can be used to mitigate differences arising from the use of different sets of process parameters without necessarily incurring recrystallization. Thus, we expect that similar outcomes can be induced in parts built with other combinations of process parameters, such as scanning speed [39,69,87,94], laser power [39,69,87], hatch spacing [36,39,87], layer thickness [87], or layer remelting [28,36]. However, it must be noted that further research is required over broader ranges of parameters to confirm the general validity of this protocol.

4. Conclusions

The scanning strategy is one of the main process parameters known to affect the microstructural aspects of PBF-LB materials, such as crystallographic texture and residual stress, primarily through its effect on the thermal history. The effect of two scanning strategies (67° rotations (ROT) and alternating 0°/67° scans (ALT)) in the heat-treated microstructure is investigated by means of *in situ* time-resolved synchrotron XRD and *ex situ* electron microscopy (ECCI, EBSD, EDS, and TEM). The key findings can be summarized as follows.

- A novel Rietveld refinement-based approach was developed to allow quantification of the cell wall fraction based on the microsegregation contribution to the diffraction peak asymmetry (*i.e.*, the left shoulder in the γ-matrix peaks).
- As determined by this approach, the fraction of cell walls (calculated from the effect of microsegregation) differs between the two scanning strategies, being approximately 5 % higher in ALT (weight fraction), and is accompanied by a slight difference in the Laves phase fraction (0.2 % higher in ALT, weight fraction).
- The *in situ* synchrotron experiment showed that peak asymmetry and the associated microsegregation decreased rapidly above 750 °C and vanished just before 900 °C during the temperature ramp-up to the isothermal solution treatment in both samples, indicating that the asymmetry is mainly controlled by the diffusion of Nb and Mo atoms.
- The Laves phase content starts diminishing in the range 800–900 °C, and the peaks disappear just below 1000 °C. It is suspected that some small and sparsely distributed Laves particles could remain in the two materials, below the detection limit of high-resolution synchrotron XRD.
- During the isothermal hold at 1027 °C for 1 h, the FWHM of both samples is further reduced only during the first 10 min.
- SEM-EDS analysis confirms the homogenization of the microsegregation in both samples after the heat treatment.
- EBSD-KAM angle distributions indicate higher levels of misorientations in the as-built ALT specimen, compared to ROT. This misorientation difference is evened out after heat treatment.
- Dilatometry was used as a viable alternative to determine the temperatures experienced by the specimens during the time-resolved *in situ* synchrotron XRD experiments performed without spot-welded thermocouples.

The method introduced in this study enables quantitative characterization of cell walls, a key microstructural feature that enhances strength in additively manufactured metals. The knowledge gained from it can contribute towards microstructure design and improved heat treatments for PBF-LB/M/IN718.

CRediT authorship contribution statement

BF: Conceptualization, Methodology, Analysis, Investigation, Visualization, Writing – original draft, Writing – review & editing. AFa: Methodology, Formal analysis, Writing – original draft, Writing – review & editing. DS: Resources. AFi: Investigation, Validation, Writing – review & editing. PSO: Investigation, Writing – review & editing. TM: Investigation, Writing – review & editing. IR: Investigation. AK: Investigation, Writing – review & editing. RDK: Funding acquisition, Writing – review & editing. GB: Writing – review & editing. AE: Supervision, Writing – review & editing. GR: Supervision, Writing – review & editing. LAJ: Conceptualization, Investigation, Supervision, Project administration, Funding acquisition, Writing – original draft, Writing – review & editing. ISM: Conceptualization, Investigation, Supervision, Project administration, Funding acquisition, Writing – original draft, Writing – review & editing.

Declaration of competing interest

The authors declare that they have no known competing financial interests or personal relationships that could have appeared to influence the work reported in this paper.

Acknowledgements

The authors express their gratitude towards the ESRF ID22 team for the support during the synchrotron experiments (experiment MA-5212). Gero Fey (BAM) is also acknowledged for the assistance with dilatometry tests, as well as Aleksander Kostka (Ruhr-Universität Bochum) for the ECCI analysis. Thanks are due to Dr. Carlos Enrique Abad Andrade (BAM) for performing the chemical analyses. The authors equally acknowledge BAM for the use of electron microscopy facilities within the Virtual Center for Electron Microscopy and the funding of this project (MIT1-IE2117).

Appendix A. Supplementary data

Supplementary data to this article can be found online at https://doi.org/10.1016/j.jmrt.2025.11.214.

Data availability

Data will be made available upon request.

References

[1] Volpato GM, Tetzlaff U, Fredel MC. A comprehensive literature review on laser powder bed fusion of inconel superalloys. Addit Manuf Jul. 2022;55:102871. https://doi.org/10.1016/j.addma.2022.102871.

[2] Rowe RA, Holtham N, Allison P, Palazotto A, Davami K. A comparison of high strain rate response and adiabatic shear band formation in additively and traditionally manufactured inconel 718. Mater Char Jan. 2024;207:113506. https://doi.org/10.1016/j.matchar.2023.113506.

[3] Zhou Y, et al. Predicting intergranular stress corrosion cracking of stainless steels in high-temperature water by incorporating crystallographic factor. Acta Mater Sep. 2025;297:121322. https://doi.org/10.1016/j.actamat.2025.121322.

[4] DebRoy T, et al. Additive manufacturing of metallic components – process, structure and properties. Prog Mater Sci Mar. 2018;92:112–224. https://doi.org/10.1016/j.pmatsci.2017.10.001.

[5] Godec M, et al. Hybrid additive manufacturing of inconel 718 for future space applications. Mater Char Feb. 2021;172:110842. https://doi.org/10.1016/j.matchar.2020.110842.

[6] Zhang D, Feng Z, Wang C, Wang W, Liu Z, Niu W. Comparison of microstructures and mechanical properties of inconel 718 alloy processed by selective laser melting and casting. Mater Sci Eng, A May 2018;724:357–67. https://doi.org/10.1016/j.msea.2018.03.073.

[7] Zhao Y, Guo Q, Ma Z, Yu L. Comparative study on the microstructure evolution of selective laser melted and wrought IN718 superalloy during subsequent heat treatment process and its effect on mechanical properties. Mater Sci Eng, A Jul. 2020;791:139735. https://doi.org/10.1016/j.msea.2020.139735.

[8] Zhao Y, Li K, Gargani M, Xiong W. A comparative analysis of inconel 718 made by additive manufacturing and suction casting: microstructure evolution in homogenization. Addit Manuf Dec. 2020;36:101404. https://doi.org/10.1016/j.addma.2020.101404.

[9] T. Kikukawa, Ishimoto ,Takuya, Kim ,Hyoung Seop, and T. Nakano, 'Remarkable strengthening effects of cells in laser powder bed fusion-processed inconel 718', Materials Research Letters, vol. 0, no. 0, pp. 1–7, doi: 10.1080/21663831.2025.2522801.

[10] Zhou Y, et al. Integrated effects of non-equilibrium microstructures on stress corrosion cracking susceptibility of post-treated laser powder-bed-fusion 316 L stainless steels. Corros Sci Aug. 2025;252:112974. https://doi.org/10.1016/j.corsci.2025.112974.

[11] Zhang F, et al. Homogenization kinetics of a nickel-based superalloy produced by powder bed fusion laser sintering. Scr Mater Apr. 2017;131:98–102. https://doi.org/10.1016/j.scriptamat.2016.12.037.

[12] Zhang S, et al. Effect of grain boundary irregularity on impact toughness in inconel 718 alloy fabricated by laser powder bed fusion. Mater Char Sep. 2025;227:115298. https://doi.org/10.1016/j.matchar.2025.115298.

[13] Deng D, Peng RL, Brodin H, Moverare J. Microstructure and mechanical properties of inconel 718 produced by selective laser melting: sample orientation dependence and effects of post heat treatments. Mater Sci Eng, A Jan. 2018;713:294–306. https://doi.org/10.1016/j.msea.2017.12.043.

[14] Zhang S, Wang L, Lin X, Yang H, Huang W. The formation and dissolution mechanisms of laves phase in inconel 718 fabricated by selective laser melting compared to directed energy deposition and cast. Compos B Eng Jun. 2022;239:109994. https://doi.org/10.1016/j.compositesb.2022.109994.

[15] Wang X, Chou K. The effects of stress relieving heat treatment on the microstructure and residual stress of inconel 718 fabricated by laser metal powder bed fusion additive manufacturing process. J Manuf Process Dec. 2019;48:154–63. https://doi.org/10.1016/j.jmapro.2019.10.027.

[16] Ferreri NC, Vogel SC, Knezevic M. Determining volume fractions of γ, γ′, γ″, δ, and MC-carbide phases in inconel 718 as a function of its processing history using an advanced neutron diffraction procedure. Mater Sci Eng, A Apr. 2020;781:139228. https://doi.org/10.1016/j.msea.2020.139228.

[17] Chlebus E, Gruber K, Kuźnicka B, Kurzac J, Kurzynowski T. Effect of heat treatment on the microstructure and mechanical properties of inconel 718 processed by selective laser melting. Mater Sci Eng, A Jul. 2015;639:647–55. https://doi.org/10.1016/j.msea.2015.05.035.

[18] Naskar S, Suryakumar S, Panigrahi BB. Post-processing of inconel 718 superalloy by Laser-based powder bed fusion: microstructures and properties evaluation. Mater Sci Eng, A Jan. 2025;921:147601. https://doi.org/10.1016/j.msea.2024.147601.

[19] Jiang R, et al. Effect of heat treatment on microstructural evolution and hardness homogeneity in laser powder bed fusion of alloy 718. Addit Manuf Oct. 2020;35:101282. https://doi.org/10.1016/j.addma.2020.101282.

[20] Čapek J, Polatidis E, Casati N, Pederson R, Lyphout C, Strobl M. Influence of laser powder bed fusion scanning pattern on residual stress and microstructure of alloy 718. Mater Des Sep. 2022;221:110983. https://doi.org/10.1016/j.matdes.2022.110983.

[21] Amato KN, et al. Microstructures and mechanical behavior of inconel 718 fabricated by selective laser melting. Acta Mater Mar. 2012;60(5):2229–39. https://doi.org/10.1016/j.actamat.2011.12.032.

[22] Tucho WM, Cuvillier P, Sjolyst-Kverneland A, Hansen V. Microstructure and hardness studies of inconel 718 manufactured by selective laser melting before and after solution heat treatment. Mater Sci Eng, A Mar. 2017;689:220–32. https://doi.org/10.1016/j.msea.2017.02.062.

[23] Newell DJ, et al. Mitigation of scan strategy effects and material anisotropy through supersolvus annealing in LPBF IN718. Mater Sci Eng, A Sep. 2019;764:138230. https://doi.org/10.1016/j.msea.2019.138230.

[24] Serrano-Munoz I, et al. The residual stress in as-built laser powder bed fusion IN718 alloy as a consequence of the scanning strategy induced microstructure. Sci Rep Sep. 2020;10(1):14645. https://doi.org/10.1038/s41598-020-71112-9.

[25] Parry L, Ashcroft IA, Wildman RD. Understanding the effect of laser Scan strategy on residual stress in selective laser melting through thermo-mechanical simulation. Addit Manuf Oct. 2016;12:1–15. https://doi.org/10.1016/j.addma.2016.05.014.

[26] Schröder J, et al. Impact of scan strategy on principal stresses in laser powder bed fusion. Mater Des Aug. 2024;244:113171. https://doi.org/10.1016/j.matdes.2024.113171.

[27] Serrano-Munoz I, et al. On the interplay of microstructure and residual stress in LPBF IN718. J Mater Sci Mar. 2021;56(9):5845–67. https://doi.org/10.1007/s10853-020-05553-y.

[28] Pant P, et al. A study of the influence of novel scan strategies on residual stress and microstructure of L-shaped LPBF IN718 samples. Mater Des Feb. 2022;214:110386. https://doi.org/10.1016/j.matdes.2022.110386.

[29] Wan HY, Zhou ZJ, Li CP, Chen GF, Zhang GP. Effect of scanning strategy on grain structure and crystallographic texture of inconel 718 processed by selective laser melting. J Mater Sci Technol Oct. 2018;34(10):1799–804. https://doi.org/10.1016/j.jmst.2018.02.002.

[30] Tao P, Li H, Huang B, Hu Q, Gong S, Xu Q. The crystal growth, intercellular spacing and microsegregation of selective laser melted inconel 718 superalloy. Vacuum Jan. 2019;159:382–90. https://doi.org/10.1016/j.vacuum.2018.10.074.

[31] Wang X, Nadimpalli VK, Tiedje NS, Juul Jensen D, Yu T. Additive-manufacturing-induced cell structure in stainless steel 316L: 3D morphology and formation mechanism. Metall Mater Trans A Feb. 2025;56(2):506–17. https://doi.org/10.1007/s11661-024-07644-w.

[32] Rielli VV, Piglione A, Pham M-S, Primig S. On the detailed morphological and chemical evolution of phases during laser powder bed fusion and common post-processing heat treatments of IN718. Addit Manuf Feb. 2022;50:102540. https://doi.org/10.1016/j.addma.2021.102540.

[33] Uenal T, Gahn L, Kittel J, Gasser A, Schleifenbaum J. Process development for tip repair of complex shaped turbine blades with IN718. Procedia Manuf Dec. 2020;47:1050–7. https://doi.org/10.1016/j.promfg.2020.04.114.

[34] Furbino M, Del Olmo R, Revilla RI, De Graeve I. Corrosion behavior of steel parts repaired using additive manufacturing: overview and research perspective. Mater Des Apr. 2025;252:113769. https://doi.org/10.1016/j.matdes.2025.113769.

[35] Chen Y, Yin Y, Yi M. Additive manufacturing repair of titanium with surface damage: molecular dynamics study on microstructure and mechanical properties. Soc Sci Res Netw Dec. 01, 2023:4650879. https://doi.org/10.2139/ssrn.4650879. Rochester, NY.

[36] Gao S, et al. Additive manufacturing of alloys with programmable microstructure and properties. Nat Commun Oct. 2023;14(1):6752. https://doi.org/10.1038/s41467-023-42326-y.

[37] Tammas-Williams S, Todd I. Design for additive manufacturing with site-specific properties in metals and alloys. Scr Mater Nov. 2016;135:105–10. https://doi.org/10.1016/j.scriptamat.2016.10.030.

[38] Ferreira AA, Reis AR, Sousa JP, Cruz JM, Vieira MF. Inconel 625/NiCrWMo functionally graded materials manufactured by direct laser deposition. Mater Char Apr. 2025;222:114862. https://doi.org/10.1016/j.matchar.2025.114862.

[39] Kasperovich G, Gussone J, Requena G, Schell N, Stark A, Haubrich J. Tailoring the strength of inconel 718: insights into LPBF parameters and heat treatment synergy. Mater Des Feb. 2025;250:113627. https://doi.org/10.1016/j.matdes.2025.113627.

[40] Radavich JF. The physical metallurgy of cast and wrought alloy 718. In: Superalloys 718 metallurgy and applications. TMS; 1989. p. 229–40. https://doi.org/10.7449/1989/Superalloys_1989_229_240. 2004.

[41] F42 committee, for additive manufacturing post processing methods standard specification for thermal post-processing metal parts made via powder bed fusion. doi: 10.1520/F3301-18A.

[42] G. M. Volpato et al., 'Revealing the γ′ and γ″ phase fractions of additively manufactured and differently heat-treated nickel-base superalloy IN718 by atom probe tomography and their impact on mechanical properties', Adv Eng Mater, vol. n/a, no. n/a, p. 2401954, doi: 10.1002/adem.202401954.

[43] Ajay P, Dabhade VV. Heat treatments of inconel 718 nickel-based superalloy: a review. Met Mater Int Nov. 2024. https://doi.org/10.1007/s12540-024-01812-8.

[44] A. Alafaghani, 'modified solution annealing heat treatments of powder bed fused inconel 718 | Research Square'. Accessed: March. 6, 2025. [Online]. Available: https://www.researchsquare.com/article/rs-718605/v1.

[45] Cao M, et al. The effect of homogenization temperature on the microstructure and high temperature mechanical performance of SLM-Fabricated IN718 alloy. Mater Sci Eng, A Jan. 2021;801:140427. https://doi.org/10.1016/j.msea.2020.140427.

[46] Schneider J, Lund B, Fullen M. Effect of heat treatment variations on the mechanical properties of inconel 718 selective laser melted specimens. Addit Manuf May 2018;21:248–54. https://doi.org/10.1016/j.addma.2018.03.005.

[47] Ding Z, et al. Achieving balanced mechanical properties in laser powder bed fusion processed inconel 718 superalloy through a simplified heat treatment process. J Mater Sci Technol May 2025;218:54–70. https://doi.org/10.1016/j.jmst.2024.06.057.

[48] Gallmeyer TG, Moorthy S, Kappes BB, Mills MJ, Amin-Ahmadi B, Stebner AP. Knowledge of process-structure-property relationships to engineer better heat treatments for laser powder bed fusion additive manufactured inconel 718. Addit Manuf Jan. 2020;31:100977. https://doi.org/10.1016/j.addma.2019.100977.

[49] Kouraytem N, et al. A recrystallization heat-treatment to reduce deformation anisotropy of additively manufactured inconel 718. Mater Des Jan. 2021;198:109228. https://doi.org/10.1016/j.matdes.2020.109228.

[50] Karabulut Y, Tascioglu E, Kaynak Y. Heat treatment temperature-induced microstructure, microhardness and wear resistance of inconel 718 produced by selective laser melting additive manufacturing. Optik Feb. 2021;227:163907. https://doi.org/10.1016/j.ijleo.2019.163907.
[51] Godec M, Zaefferer S, Podgornik B, Šinko M, Tchernychova E. Quantitative multiscale correlative microstructure analysis of additive manufacturing of stainless steel 316L processed by selective laser melting. Mater Char Feb. 2020; 160:110074. https://doi.org/10.1016/j.matchar.2019.110074.
[52] Čapek J, et al. The effect of γ″ and δ phase precipitation on the mechanical properties of inconel 718 manufactured by selective laser melting: an in situ neutron diffraction and acoustic emission study. JOM Jan. 2021;73(1):223–32. https://doi.org/10.1007/s11837-020-04463-3.
[53] Solís C, et al. In situ characterization at elevated temperatures of a new Ni-Based superalloy VDM-780 premium. Metall Mater Trans A Sep. 2018;49(9):4373–81. https://doi.org/10.1007/s11661-018-4761-6.
[54] Mote V, Purushotham Y, Dole B. Williamson-hall analysis in estimation of lattice strain in nanometer-sized ZnO particles. J Theor Appl Phys Jul. 2012;6(1):6. https://doi.org/10.1186/2251-7235-6-6.
[55] Borbély A. The modified williamson-hall plot and dislocation density evaluation from diffraction peaks. Scr Mater Aug. 2022;217:114768. https://doi.org/10.1016/j.scriptamat.2022.114768.
[56] Schneiderman B, Chuang AC, Kenesei P, Yu Z. In situ synchrotron diffraction and modeling of non-equilibrium solidification of a MnFeCoNiCu alloy. Sci Rep Mar. 2021;11(1):5921. https://doi.org/10.1038/s41598-021-85430-z.
[57] Fitch A, et al. ID22 – the high-resolution powder-diffraction beamline at ESRF. J Synchrotron Radiat Jul. 2023;30:1003–12. https://doi.org/10.1107/S1600577523004915.
[58] Seto Y, Nishio-Hamane D, Nagai T, Sata N. Development of a software suite on X-ray diffraction experiments. Rev High Pres Sci Technol Aug. 2010;20:269–76. https://doi.org/10.4131/jshpreview.20.269.
[59] Coelho A. TOPAS and TOPAS-Academic: an optimization program integrating computer algebra and crystallographic objects written in C++. J Appl Crystallogr Feb. 2018;51:210–8. https://doi.org/10.1107/S1600576718000183.
[60] Bachmann F, Hielscher R, Schaeben H. Grain detection from 2d and 3d EBSD data—Specification of the MTEX algorithm. Ultramicroscopy Dec. 2011;111(12): 1720–33. https://doi.org/10.1016/j.ultramic.2011.08.002.
[61] del Gaudio J, et al. Grain size assessment using EBSD on heterogeneous additively manufactured microstructures. IOP Conf Ser Mater Sci Eng Aug. 2024;1310(1): 012028. https://doi.org/10.1088/1757-899X/1310/1/012028.
[62] Hielscher R, Silbermann CB, Schmidl E, Ihlemann J. Denoising of crystal orientation maps. J Appl Crystallogr Oct. 2019;52(5):984–96. https://doi.org/10.1107/S1600576719009075.
[63] Field DP, Bradford LT, Nowell MM, Lillo TM. The role of annealing twins during recrystallization of Cu. Acta Mater Jul. 2007;55(12):4233–41. https://doi.org/10.1016/j.actamat.2007.03.021.
[64] Rui S-S, et al. Correlations between two EBSD-Based metrics kernel average misorientation and image quality on indicating dislocations of near-failure low alloy steels induced by tensile and cyclic deformations. Mater Today Commun Jun. 2021;27:102445. https://doi.org/10.1016/j.mtcomm.2021.102445.
[65] Serrano-Munoz I, Fernández R, Saliwan-Neumann R, González-Doncel G, Bruno G. Dislocation substructures in pure aluminium after creep deformation as studied by electron backscatter diffraction. J Appl Crystallogr Aug. 2022;55(4):860–9. https://doi.org/10.1107/S1600576722005209.
[66] Schindelin J, et al. Fiji: an open-source platform for biological-image analysis. Nat Methods Jul. 2012;9(7):676–82. https://doi.org/10.1038/nmeth.2019.
[67] Zhou L, Mehta A, McWilliams B, Cho K, Sohn Y. Microstructure, precipitates and mechanical properties of powder bed fused inconel 718 before and after heat treatment. J Mater Sci Technol Jun. 2019;35(6):1153–64. https://doi.org/10.1016/j.jmst.2018.12.006.
[68] Upadhyay M, Gaudez S, Pantleon K. Dislocation structure evolution during metal additive manufacturing. IOP Conf Ser Mater Sci Eng Aug. 2024;1310:012012. https://doi.org/10.1088/1757-899X/1310/1/012012.
[69] Deng H, et al. Orientation dependence of microstructure and mechanical property in selective laser-melted inconel 718 alloy. Mater Char Feb. 2025;220:114664. https://doi.org/10.1016/j.matchar.2024.114664.
[70] Obana M, Prasad K, Ito A, Torizuka S. The possible role of nano sized precipitates on the mechanical properties of additively manufactured IN 718 superalloy. Mater Sci Eng, A 2021;826:141972. https://doi.org/10.1016/j.msea.2021.141972. Oct.
[71] Nayir S, et al. Effect of homogenization heat treatment on the evolution of carbonitrides in powder bed fusion processed INCONEL 718. Mater Char Sep. 2025;227:115271. https://doi.org/10.1016/j.matchar.2025.115271.
[72] Schröder J, et al. On the influence of heat treatment on microstructure and mechanical behavior of laser powder bed fused inconel 718. Mater Sci Eng, A Feb. 2021;805:140555. https://doi.org/10.1016/j.msea.2020.140555.
[73] Messé OMDM, Muñoz-Moreno R, Illston T, Baker S, Stone HJ. Metastable carbides and their impact on recrystallisation in IN738LC processed by selective laser melting. Addit Manuf Aug. 2018;22:394–404. https://doi.org/10.1016/j.addma.2018.05.030.
[74] Naim Katea S, Tai C-W, Ström P, Larsson P-O, Vidarsson H, Westin G. Niobium carbide – nickel-Niobium alloy composites from a nickel coated powder: microstructural development during sintering. Open Ceramics Jun. 2021;6: 100096. https://doi.org/10.1016/j.oceram.2021.100096.
[75] E37 Committee, Test method for linear thermal expansion of solid materials with a push-rod dilatometer. doi: 10.1520/E0228-22.
[76] Morocoima M, Quintero M, Guerrero E, Tovar R, Conflant P. Temperature variation of lattice parameters and thermal expansion coefficients of the compound ZnGa2Se4. J Phys Chem Solid Mar. 1997;58(3):503–7. https://doi.org/10.1016/S0022-3697(96)00048-0.
[77] Pröbstle M, et al. Superior creep strength of a nickel-based superalloy produced by selective laser melting. Mater Sci Eng, A Sep. 2016;674:299–307. https://doi.org/10.1016/j.msea.2016.07.061.
[78] Toby BH. R factors in rietveld analysis: how good is good enough? Powder Diffr Mar. 2006;21(1):67–70. https://doi.org/10.1154/1.2179804.
[79] Ni M, Liu S, Chen C, Li R, Zhang X, Zhou K. Effect of heat treatment on the microstructural evolution of a precipitation-hardened superalloy produced by selective laser melting. Mater Sci Eng, A Mar. 2019;748:275–85. https://doi.org/10.1016/j.msea.2019.01.109.
[80] Li X, et al. Effect of heat treatment on microstructure evolution of inconel 718 alloy fabricated by selective laser melting. J Alloys Compd Oct. 2018;764:639–49. https://doi.org/10.1016/j.jallcom.2018.06.112.
[81] Schröder J, et al. Understanding the impact of texture on the micromechanical anisotropy of laser powder bed fused inconel 718. J Mater Sci Aug. 2022;57(31): 15036–58. https://doi.org/10.1007/s10853-022-07499-9.
[82] Sutter JP, Baron AQR, Ishikawa T, Yamazaki H. Examination of bragg backscattering from crystalline quartz. J Phys Chem Solid Dec. 2005;66(12): 2306–9. https://doi.org/10.1016/j.jpcs.2005.09.044.
[83] Tucho W, Hansen V. Studies of post-fabrication heat treatment of L-PBF-Inconel 718: effects of hold time on microstructure, annealing twins, and hardness. Metals 2021;11:266. https://doi.org/10.3390/met11020266. Feb.
[84] Ungár T. Dislocation densities, arrangements and character from X-ray diffraction experiments. Mater Sci Eng, A Jul. 2001;309(310):14–22. https://doi.org/10.1016/S0921-5093(00)01685-3.
[85] Sugiyama S, Ogawa T, He L, Wang Z, Adachi Y. Quantitative analysis of the recovery process in pure iron using X-ray diffraction line profile analysis. Materials Jan. 2021;14(4). https://doi.org/10.3390/ma14040895. 4.
[86] J. C. Pereira, 'Analysis of microstructure and mechanical properties in as-built/as-cast and heat-treated conditions for IN718 alloy obtained by selective laser melting and investment casting processes'. Accessed: March. 6, 2025. [Online]. Available: https://www.mdpi.com/2073-4352/11/10/1196.
[87] Ghorbanpour S, et al. Additive manufacturing of functionally graded inconel 718: effect of heat treatment and building orientation on microstructure and fatigue behaviour. J Mater Process Technol Aug. 2022;306:117573. https://doi.org/10.1016/j.jmatprotec.2022.117573.
[88] Prakash T, Bauri R. Investigation on microstructural and texture evolution in additive friction stir deposited inconel 718 alloy. Mater Char Jul. 2025;225: 115088. https://doi.org/10.1016/j.matchar.2025.115088.
[89] Pathak A, Singh AK. Mechanical properties of Ni-based solid solution alloys: a first principles study. J Appl Res Technol Oct. 2017;15(5):449–53. https://doi.org/10.1016/j.jart.2017.05.006.
[90] Lei P, et al. Corrosion behavior of Ni-Cr alloys with different Cr contents in NaCl-KCl-MgCl2. Materials Jan. 2024;17(10). https://doi.org/10.3390/ma17102335. 10.
[91] Leinders G, Cardinaels T, Binnemans K, Verwerft M. Accurate lattice parameter measurements of stoichiometric uranium dioxide. J Nucl Mater Apr. 2015;459: 135–42. https://doi.org/10.1016/j.jnucmat.2015.01.029.
[92] J. Schröder, 'Diffraction-based residual stress characterization in laser additive manufacturing of metals'. Accessed: March. 6, 2025. [Online]. Available: https://www.mdpi.com/2075-4701/11/11/1830.
[93] Dubiel B, et al. Effect of high temperature annealing on the microstructure evolution and hardness behavior of the inconel 625 superalloy additively manufactured by laser powder bed fusion. Archiv Civ Mech Eng Oct. 2023;23(4): 249. https://doi.org/10.1007/s43452-023-00787-4.
[94] Liu SY, Li HQ, Qin CX, Zong R, Fang XY. The effect of energy density on texture and mechanical anisotropy in selective laser melted inconel 718. Mater Des Jun. 2020; 191:108642. https://doi.org/10.1016/j.matdes.2020.108642.